FORSCHUNGSZENTRUM JÜLICH GmbH

Institut für Plasmaphysik
Association EURATOM-KFA

Investigation of E × B Transport with a Multi-Electrode Probe in the Plasma Boundary of TEXTOR

First Results

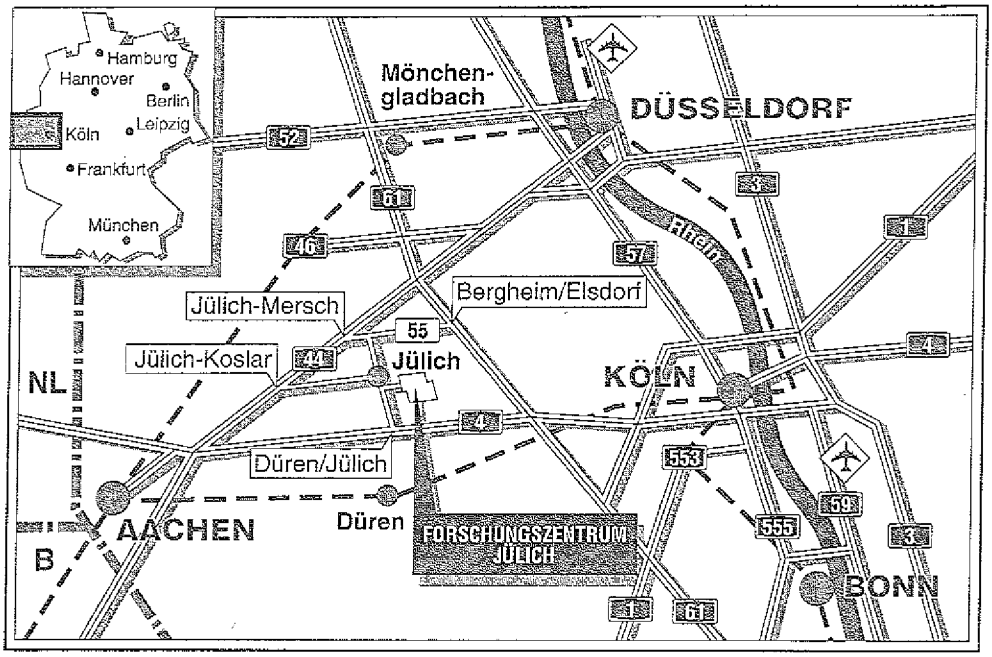

Berichte des Forschungszentrums Jülich ; 2432
ISSN 0366-0885
Institut für Plasmaphysik Jül-2432
Association EURATOM-KFA

Zu beziehen durch: Forschungszentrum Jülich GmbH · Zentralbibliothek
Postfach 1913 · D-5170 Jülich · Bundesrepublik Deutschland
Telefon: 02461/61-6102 · Telefax: 02461/61-6103 · Telex: 833556-70 kfa d

Investigation of E × B Transport with a Multi-Electrode Probe in the Plasma Boundary of TEXTOR

First Results

R.S. Ivanov[1], D. Bora[2], G. Fuchs
K. Höthker, R.A. Moyer[3], U. Samm
R. van Nieuwenhove[4], G. van Oost[4]

Institut für Plasmaphysik, Forschungszentrum Jülich GmbH, Association EURATOM-KFA
[1] Institute for High Temperatures, Academy of Sciences, Moscow
[2] Institute for Plasma Research, Bhat, Gandhinagar-382424, India
[3] Institute of Plasma and Fusion Research University of California, Los Angeles, CA 90024
[4] Laboratoire de Physique des Plasmas Laboratorium voor Plasmafysica,
Association EURATOM - Etat Belge - Associatie EURATOM - Belgische Staat,
Ecole Royale Militaire - Koninklijke Militaire School, B-1040 Brussels

Abstract

A movable multi–element Langmuir probe was implemented in TEXTOR in order to study properties of the edge and scrape–off plasma. The probe has five graphite electrode pins allowing the simultaneous measurement of main plasma parameters such as plasma densities, electron temperatures, floating potentials, poloidal and radial electric fields. Both time–averaged and fluctuating quantities have been considered in order to evaluate the DC and turbulence–driven cross-field particle fluxes. The spectral analysis of the fluctuating floating potentials at spatially separated probe pins allows to determine the velocity associated with the rotations of the boundary plasma. The investigations have been focused on the variations of plasma boundary properties in plasmas with pure ohmic heating as well as auxiliary heating (ICRH). Special attention has been paid to the change of transport properties with the transition to a detached plasma. In particular, a significant reduction of the poloidal phase velocity at the limiter edge has been observed for detached plasmas. Preliminary data on physical effects near the plasma boundary, which occur when the toroidal belt limiter (ALT–II) is biased, are reported.

Table of contents

1 INTRODUCTION

Experiments on the TEXTOR tokamak are mainly devoted to the investigation of plasma wall interaction. Good access for diagnostics through a large number of ports and a flexible limiter system provide excellent experimental conditions. Comprehensive plasma edge diagnostics are installed, which allow e.g. measurements of particle fluxes or profiles of electron density and temperature with high spatial resolution at various locations at the plasma boundary [1, 2, 3].

A central topic of plasma boundary research is the transport of particles and energy. In particular, the mechanisms leading to anomalously high transport across the magnetic field have to be investigated. The anomalous transport is generally attributed to microscopic plasma turbulence [4, 5]. There is only little conclusive evidence for the cause of this turbulence (e.g. drift modes), thus more experimental data on fluctuation induced transport is needed.
An experimental programme for the investigation of fluctuation induced transport has been started on TEXTOR. In a previous work, measurements of density fluctuations have already been obtained with an atomic probing beam [6]. In collaboration with the Institute for High Temperatures (IVTAN) Moscow, a multi–electrode probe has been developed and installed in TEXTOR in order to provide data on electric potentials, radial, poloidal and toroidal electric fields, ion saturation currents, electron density and electron temperature. The experimental capabilities of this probe and first results are described in this report.

In section 2, the experimental set–up and the methods of signal extraction and processing are described. Preliminary experimental results obtained under various discharge conditions (ohmic heating, ICRH heating, density variations, limiter biasing) are given in section 3. Conclusions and prospects of future work are presented in section 4.

2 EXPERIMENTAL SET–UP AND DATA PROCESSING

2.1 General features of TEXTOR

The Torus Experiment for Technology–Oriented Research (TEXTOR) is a long pulse (greater than 3 sec) medium–sized tokamak, primarily used for systematic studies of plasma–wall interaction. Figs.1–3 display the geometry of TEXTOR. The main parameters of TEXTOR are : major radius $R = 1.75$ m, minor radius $a = 0.46$ m, toroidal field $B_t \leq 2.6$ Tesla, plasma current $I_p \leq 500$ kA.

TEXTOR is equipped with different types of limiters. The poloidal limiters are composed of three movable graphite segments as shown in Fig.2. The reference limiters,indicated in Fig. 2, are semi–spherically shaped. Graphite tiles are used to protect the inner side of the torus. A liner serves as a surface around the torus, which is, however, interrupted by many portholes required for pumping, diagnostics etc. ALT–II is an axisymmetric toroidal belt limiter, composed of 8 graphite blades, used as the main limiter during our experiments. ALT–II is supported through several portholes which are also used for pumping. The poloidal location of ALT–II is shown in Fig.3. Generally, all plasma facing surfaces are carbonized or boronized [7].

Radio–frequency heating near the ion cyclotron frequency (ICRH) and neutral beam injection (NBI) are used as auxiliary heating methods. RF power up to the 4 MW is applied by two π–shifted pairs of fast wave antennas separated toroidally by 180 degrees. The generator frequency is 32.5 MHz. The antennas are mounted with side protection limiters and they can be moved radially by 10 cm. Two neutral beam injectors (NBI), co– and counter–injection with respect to the plasma current, can provide a total of 3.4 MW additional heating power.

2.2 The electric probe

An array of electric probes was inserted into the plasma through the diagnostic port located at the outboard midplane of TEXTOR (Fig.2). The probe system can be moved radially on a shot to shot basis. The accuracy of the relative radial position of the probes is 0.1 cm, while the accuracy of absolute positioning is estimated to be about 0.3 cm. Due to an uncertainty caused by thermal expansion of the supporting structure the position of the probe system with respect to ALT–II is known within an accuracy of about 0.5 cm. The probe array is composed of five electrode pins spaced poloidally, radially and toroidally. The arrangement of the multi–element probe is displayed in Fig.4. Three of the pins have been used for the measurement of the poloidal and the radial electric fields. The other two pins are necessary for the measurement of plasma density n_e and electron temperature T_e. The poloidal separation of the probes used for the measurement of poloidal electric fields is 1 cm and the radial separation of the pair of pins used for the radial electric field measurements is 0.2 cm. This radial separation of the pins is obtained with the help of a tube insulator made of Boron–nitrite ceramics. The probe pins are made from graphite and they are two millimeters long and two millimeters in diameter. The multi–probe system is surrounded by a graphite shield of cylindrical shape and 30 mm in diameter.

2.3 Evaluation of main plasma parameters

The parameters of the plasma boundary have been measured following standard probing techniques. The plasma density and its fluctuations have been obtained from the signals of the ion saturation current collected by the single negatively biased (-100 V) probe. The procedure to obtain the density from the probe signal is the same as the one described in detail elsewhere [8]. It may be somewhat doubted, wether it gives correct values for the plasma density in the scrape–off layer of a tokamak. There is growing evidence, both theoretical and experimental, that the ion temperature in the scrape–off plasma may significantly exceed that of the electrons [9, 10, 11, 14]. Then the usual assumption namely that the perpendicular velocity of ions bombarding the probe surface to be proportional to $(kT_e)^{1/2} + eV_{sheath}$ may need to be modified. However, this requires the knowledge of the ion temperature T_i, which is not measured. A rather large ion temperature furthermore modifies the shape of the surface before the probe from which ions are collected. It may be noted that these two effects compensate each other to some extent. If the electron temperature is high enough, secondary electron emission may considerably contribute to the measured probe current. [12, 13] As far as it is only due to emission caused by electron impact, this effect does not change the ion saturation current and the electron Temperature T_e derived from the logarithmic part of the characteristic. It does, however, shift the characteristic in the direction of positive voltages and makes the determination of the plasma potential uncertain [33]. Unfortunately the secondary electron emission depends strongly on any surface layer of the pin [13], which cannot be controlled in practice. The secondary electron emission coefficient for graphite is low and its influence on the probe characteristic is discussed in [15, 24, 33], in our cases the probe current can be uncertain by a few percent. An independent measurement of the plasma density profiles in the plasma boundary based on the Lithium beam technique provides a possibility for comparison and calibration of the Langmuir probe measurements cf. Fig. 14. Nevertheless, the accuracy of relative measurements of plasma densities, such as radial profiles, are supposedly better than that of absolute values. The decay lengths of electron and ion temperatures within the scrape–off layer are larger than that of the plasma density. Therefore the error introduced by uncertainties in ion and electron temperatures does not considerably affect the radial profiles of density or fluctuation induced fluxes. This statement does not hold at the limiter edge, because the gradient of the electron temperature there is large.

The floating potential measurements are rather easy to do, unfortunately they can only provide integrated information on plasma parameters. The correct evaluation of the space potential from the floating potential measurements, however, depends on several assumptions to be made. The commonly used estimate of the sheath potential assumes a maxwellian distribution of electron velocities and neglects secondary electron emission. While the first assumption seems to be valid in the boundary plasma there is a strong evidence [12, 13, 14] that the later is not quite true, especially if the electron temperature markedly exceeds 10 eV. Since the drop of the sheath potential ($V_s \simeq 3kT_e$ see discussion in [24]) usually dominates the floating potential, the uncertainties in its evaluation may strongly hamper the calculation of the space potential from the floating potential. From this point of view the determination of the radial electric field profiles from the measured radial profiles of floating potential and electron temperature is questionable and serves only as a rough and qualitative approximation. For the proper evaluation of the radial electric fields direct measurements of the space potential are necessary.

Only in the absence of gradients in the electron temperature, the electric field deduced from the floating potentials are true. This could also apply to poloidal fields.

2.4 Oscillatory technique for the electron temperature measurement

Because of the difficulties to measure the electron temperature with double and triple probes [18, 19], we employed another method, which works with a single probe and therefore is not troubled by DC electric fields [16, 17]. This method uses the nonlinearity of the Langmuir probe characteristic, which causes a DC offset to the floating potential, when a small AC voltage is applied to the probe. As the curvature is a function of the electron temperature this is true also for the offset. It has been shown [18] that a sinusoidal voltage U_0 applied to the probe increases its current by a factor $I_0(U_0/T_e)$ [9] where I_0 is the modified Bessel function. This holds for an exponential probe characteristic, which in turn assumes a maxwellian distribution function for the electrons. The extra current to the probe then causes a shift of the floating potential given by $\Delta\phi = T_e \times ln[I_0(U_0/T_e)]$, from which the electron temperature is calculated.

To avoid experimental errors, the impedance of the oscillator has to be low as compared to the probe sheath impedance, favouring small probes. This method has already been tested experimentally [20, 21]. The calculation of T_e from the measurement is easier for small superimposed signals, because we may then just use the first term of the expansion [20, 21]

$$\Delta\phi_{fl} = -U_0 \left[\frac{U_0}{4T_e} - \frac{1}{64} \left(\frac{U_0}{T_e} \right)^3 + \ldots.. \right] \tag{1}$$

giving

$$\Delta\phi_{fl} \approx \frac{-U_0^2}{4T_e} \tag{2}$$

In practice one can overlay rectangular wave packets on the probe voltage and compare the floating potential in the modulated phase of the bunch to the unmodulated one. The experimental results from TF–1, where this technique was used gave good agreement to those from the triple probe [22].

We employed a similar technique on TEXTOR. The schematic diagram of the electric circuit is shown in Fig. 5. Bunches of 500 kHz sine-waves have been generated with a standard Wavetec 114 function generator by gating it with a low frequency square wave from a second function generator. The duration of the gating pulses was 4–5 ms with duty factor 1. Such a pulse length is needed for a proper time averaging of the floating potential fluctuations. The oscillation frequency was chosen to 500 kHz, since it was low enough to minimize the damping in the circuit and at the same time allow further filtering of the signals. The averaging of the fluctuations has been achieved with a RC– filter with a 1 ms time constant. Typical signal picked up from the probe in TEXTOR along with the gating pulses are displayed in Fig. 6.

The advantages of the method are:

o It is simple.

o T_e is easy to calculate from the measurement.

o It is local and therefore insensitive to DC electric fields.

However, this method cannot provide information on electron temperature fluctuations with frequencies exceeding the gating frequency, thus the time resolution is limited.

2.5 Computation of DC and turbulence–driven particle fluxes

The frequency spectra of the edge turbulence usually peak at frequencies around 50–100 kHz [23]. For such large frequencies, the cross–field particle transport may be separated namely into the DC convection $\vec{\Gamma}_0$ and the fluctuation induced drift $\vec{\Gamma}_{fl}$. In the following, these particle fluxes are presented separately.

The fluctuation–induced particle fluxes $\vec{\Gamma}_{fl}$ driven by the correlated density and electric field fluctuations have been calculated in the conventional manner [8]

by averaging over a period T.

$$\vec{\Gamma}_{fl} = \frac{1}{T}\int_0^T \tilde{n}(t)\tilde{v}(t)dt \tag{3}$$

where $\tilde{v}(t) = \tilde{E}/B$ is the fluctuating drift velocity and $\tilde{E}$ is the fluctuating electric field.
Simultaneous measurements of the poloidal and radial components, E_p and E_r, of the fluctuating electric field allow the evaluation of the vector $\vec{\Gamma}$, which represents the direction of the fluctuation induced particle flux in the poloidal plane.
The uncertainity introduced by experimental errors due to possible electric fields are quite different for AC and DC components of the particle flux.
The DC convective particle flux was calculated as follows

$$\vec{\Gamma}_0 = n_e \vec{v}_0 \tag{4}$$

with

$$\vec{v}_0 = \frac{\vec{E}_0 \times \vec{B}}{B^2} \tag{5}$$

$\vec{E}_0$ is the DC electric field.
The poloidal components of both, DC and fluctuation induced fluxes, contribute to the poloidal rotation of the boundary plasma. A typical time-resolved plot of the fluctuation induced particle flux is shown in Fig.7. This plot demonstrates that the mean flux is non–zero.

2.6 Spectral analysis of plasma fluctuations, statistical dispersion relation and evaluation of the poloidal phase velocities

One of the simplest methods to study turbulence in a plasma is to register the frequency spectra of the floating potential on a single Langmuir probe. Unfortunately the physics information about the plasma gathered in this way is rather poor. This is because those measurements are performed in the laboratory frame of reference and it is then not possible to distinguish moving waves in a standing plasma from standing waves in a moving plasma. Furthermore one is unable in this case to tell the direction of wave propagation as well as the wavelength and velocity. A double probe or an array of probes provides more information. The cross–correlation function given by

$$C_{12}(\tau) = \int U_1(t)U_2(t-\tau)dt, \tag{6}$$

where U_1, U_2 are the two floating potentials, provides both the velocity of propagation v and its direction. A typical example of C_{12} is shown in Fig.8. var velocity of propagation may be derived from $v = d/\tau_d$, where d is the spacing between the probes and τ_d is the delay time of the first maximum on $C_{12}(\tau)$. However, this method does not tell whether the waves or the plasma move.
Another method to calculate v and its direction uses the cross power spectrum and its phase.

$$C_{12}(\omega) = U_1(\omega) * U_2^+(\omega), \tag{7}$$

$$\Delta\phi = \frac{ImC_{12}(\omega)}{ReC_{12}(\omega)} \tag{8}$$

where the $U(\omega)$ are the Fourier transforms of the above $U(t)$ and $^+$ indicates the conjugate complex. The phase is related to the wave number k by $k * d = \Delta\phi(\omega)$.

A typical example for the power spectrum i.e. $|C_{ij}(\omega)|$ is shown in Fig.9, whereas Fig.12 gives a typical k–spectrum.

The spectral correlation function is a real function of the two variables ω and k, it has the value $|C_{ij}(\omega)|$ in the ω–k plane. Note that we may use k rather than ϕ because they are proportional to each other as long as aliasing is disregarded. In order to calculate the complex power spectrum $C_{ij}(\omega)$ we Fourier transform the signals. To accelerate the calculations we usually used fast Fourier transform, which requires the number of data points being an integer power of 2, in most of our cases this was 8192. The Fourier transform implies periodic boundary conditions. To reduce the statistical errors we can use the technique of filtering the signals $U_i(t)$ as described in [32]. However, in case of a large number of data points (8192) the difference to the unfiltered case is rather small. After Fourier transform we calculate the cross power spectrum

$$C_{ij}(\omega, \phi) = | C_{ij}(\omega) | e^{i(\phi_i - \phi_j)} = f_i(\omega_0) f_j^*(\omega) \tag{9}$$

where $f(\omega)$ is the Fourier transform of $f(t)$. The cross power spectrum provides a fast way to calculate the cross–correlation function by Fourier back transform.

$$C_{ij}(\tau) = \int C_{ij}(\omega, \phi) e^{i\omega\tau} d\omega \tag{10}$$

This function is normalized as follows:

$$\hat{C}_{ij}(\tau) = \frac{C_{ij}(\tau)}{[C_{ii}(\tau = 0) - C_{jj}(\tau = 0)]^{1/2}} \tag{11}$$

where C_{ii} are the respective autocorrelation functions. The spectral correlation function $S(\omega, \phi)$ is the plot of $\hat{C}$, versus ω and the phase ϕ. For a finite number n of sampling points S would be a set of n/2 points above the ω–ϕ plane. For this reason it is hard to visualize, because we have a line spectrum which gives the function a needle shape. This kind of result is due to the facts that

1) We took periodic boundary conditions to extend the measuring interval to infinity.

2) We viewed the sampling interval being infinitesimally small.

Assumption 2 is, however, not realistic. If we take a finite sampling width, we get instead of the line spectrum in Fourier space the spectrum

$$f_i(\omega) = \sum f_i \frac{\sin((\omega - \omega_i)\Delta t)}{(\omega - \omega_i)\Delta t} \tag{12}$$

This means that we must replace the finite point set S by the continuous function,

$$S_{ij}(\omega, \phi) = \sum f_i f_j \frac{\sin((\omega - \omega_i)\Delta t)\sin(2\pi(\phi - \phi_j)/\Delta\phi)}{(\omega - \omega_i)\Delta t \times 2\pi(\phi - \phi_j)/\Delta\phi} \tag{13}$$

whereby we made the assumption, that we can adopt an equal spacing in ϕ–direction which, because of periodic sampling, is true in the ω direction. To get a fast overlook, it may be sufficient to plot the statistical dispersion curve, i.e. the wave number k versus ω (cf. Fig. 10,11). If there are regions where the points are gathered near a curve, the dispersion curve, we can get the group velocity $d\omega/dk$ and the phase velocity ω/k. If this is not the case, the signals from two probes are stochastic which usually indicates random noise. The statistical dispersion curve may, however, be obscured if the spectrum of fluctuations is a line spectrum with underlying noise. In such cases it is better to plot the spectral correlation function. Such an example, which uses an isocontour plot with the contour lines spaced logarithmically,

is shown in Fig.13. In this plot the large amplitudes within the spectrum are emphasized thereby making the dispersion curve better visible. A noisy region shows up on the spectral function as a rather flat area.
If $d\omega/dk$ is a constant along the isocontour (starting at $\omega = 0$; $\Phi = 0$) this means that the waves (propagating across the probes) do not show dispersion. The phase and group velocities are then equal, in (Fig. 10) they are found in the range $1...5 \times 10^5$ cm/s. The evaluation method using the spectral function still leaves us with two ambiguities, namely:
The modus of how the wave propagate remains unresolved. Although standing waves in a moving plasma give $\omega/k = d\omega/dk$, the reverse is not necessarily valid.
Due to finite probe spacing a wave number could be replaced by its integer multiple without any change in $S(\omega, k)$ (aliasing).
The plot in Fig.11a shows the example with wave number k jumping from the value of π to $-\pi$. The apparent second branch of fluctuations parallel to the first can be seen in the plot. This behaviour of the bulk dispersion is artificial and it results from "spatial aliasing" when the wave length of floating potential fluctuations becomes equal to the spacing interval between the probes. The same plot with continuous boundary conditions in phase is presented in Fig.11b. The aliasing occurs in the cases of short wavelength together with large probe spacings.
The apparent phase velocity is the sum of gradient and $E \times B$ driven drifts. In contrast to the case in TEXT [25], where the $E \times B$ drift dominates, in TEXTOR both contributions are of the same order [24]. Therefore, to obtain the poloidal rotation velocity of the plasma, we have also to determine the pressure profile. The modus of how the fluctuations propagate was identified by calculating the $E \times B$ velocity using the measured E_r and estimating the diamagnetic drift contribution from the density and electron temperature profiles assuming $T_i \approx T_e$ [5, 24].

3 EXPERIMENTAL RESULTS

Based on the experimental techniques described in section 2 the following parameters have been determined:
the time-average of floating potential $\langle U_f \rangle$,
the ion saturation current $\langle I^+ \rangle$,

the local plasma density n,
the electron temperature T_e,
the poloidal E_p and the radial E_r electric fields,
the fluctuation level of E_p and E_r (root–mean–square, rms),
the relative density fluctuation level $\tilde{n}/n$,
the DC convective Γ_0 and the particle fluxes driven by turbulence,
the maximum values of cross–correlation functions C_0
and the fluctuation phase velocities v_{ph} .

3.1 Ohmic heating

In Fig.15 the variation of various parameters near the plasma boundary are plotted versus the minor radius for standard ohmic discharges, i.e. for deuterium filling, a plasma current of 340 kA, and a central line averaged density $\overline{n}_e = 3 \times 10^{13}$ cm^{-3} The radial variation of the main parameters (n_e, T_e, U_f, E_p) agrees with those observed in other machines [16]. There is a jump of about 50 eV of the floating potential of the probe near the limiter radius. If this is not due to one of the effects discussed before (section 2.3) then it is associated with a radial electric field, which in turn causes poloidal plasma rotation [25].
Additional information about this rotation was derived from an analysis of the fluctuation measurements. The radial profile of the phase velocity obtained from the spectral function shows a large shear near the limiter edge, which even leads to a reversal of the sign of the direction of rotation. This phase velocity can be associated with a poloidal rotation of the plasma (see sections 2.5 and 2.6). The plasma in the SOL rotates in the ion diamagnetic drift direction with a velocity of about 2 km/s, while the plasma inside the separatrix rotates in the other direction with approximately the same velocity. These observations are in qualitative agreement with the measurements in TEXT [25].
The radial profile of the space potential, evaluated from $V_s = V_f + 3T_e$ where T_e and U_f are taken from (Fig.15a,b), can explain the the plasma rotation profile in the SOL at least qualitatively. A quantitative comparison with the measured poloidal velocity (Fig.15e) shows some discrepancies, which could be due to secondary electron emission influencing the measurement of sheath potential.

In Fig.16 the parallel flow velocity obtained from Mach–probe measurements are presented [27]. Both, the Mach probe measurements and the E_p measurements show a reversal of plasma flow at about the limiter radius (compare with Fig.15e). The measurements are also in rough agreement when projecting the flow parallel to $\vec{B}$ onto the poloidal plane.
The variation of the radial turbulence–driven particle flux (Fig.15k) is mainly due to a change in the correlation of the poloidal electric field fluctuations (Fig.15g), rather than to a change in the fluctuation amplitude (Fig.15i). The radial position where the fluctuations of the poloidal electric field become decorrelated is found to be the same where the flow reverses. The gradients in the radial flux profiles in the SOL (Fig.15k) show evidence for the existence of additional particle source and sink terms other than recombination at the wall. This phenomenon can be explained by the 2–d structure of the transport and possibly by macroscopic non–uniformities, as they have been observed e.g. in the boundary of the tokamak TF–1 [28]. If there exist small cells in the T_e profile as they have been found on TF–1 [28], they may, to a certain extent, effect the deduction of the DC electric field from the measured differences of the DC floating potentials. The comparison of electron temperatures on two poloidally spaced probes may help to clarify these questions.

3.2 ICRH

The effects on the plasma boundary of separately varying the radius of the energized and passive RF–antennas have been studied [24]. In one series of discharges the probes and the active antenna were kept at a fixed location, $r = 48$ cm and $r = 47$ cm respectively, and the position of the passive antenna was varied from $r = 47$ cm to $r = 52$ cm. The measured U_f and E_p values are plotted as a function of the radial position of the passive antenna in Fig.20a. Both U_f and E_p vary strongly as a function of the passive antenna radius showing the sensitivity of the electric fields to details of the limiter and antenna geometry in the SOL. In a second series, the passive antenna was fixed at $r = 52$ cm and the radial position of the active antenna was varied from $r = 47$ cm to $r = 52$ cm. Both U_f and E_p decrease steadily as the probes passed the active antenna in the direction towards smaller radii, indicating that ICRH–induced effects are strongest on field lines which intersect the antenna.

This spatial variation of DC electric fields generated by ICRH in the SOL agrees with scanning probe measurements during ICRH power modulation experiments [24]. The poloidally nonuniform sheath rectification effect along the ICRH antenna structure is probably the mechanism for the generation of E_p [26, 29]. The sensitivity of the electric field to details of the limiter geometry may arise due to the rearrangement of DC currents that flow between these structures. These currents have been measured during the radial scans of Fig.20 and will be discussed in a publication to come [29].

3.3 Density scan and detached plasma in ohmic heating

Density scans in ohmic heated plasmas have been performed in order to investigate the dependence of the cross–field transport on the plasma parameters in the boundary. The density has been changed from shot to shot and data have been taken during the flat–top phase of the discharges with the probe located at $r_p = 46$ cm and $r_p = 47$ cm. These quantities are shown in Fig.17 as a function of the line–averaged density $\overline{n}_e$. For large densities we get a detached plasma, i.e. a plasma with a cold radiative layer, almost 100% radiation cooling and with the ionization zone of the recycling neutrals being detached from the limiter [30]. Detachment develops beyond a critical density n_{ec}. This density depends on the impurity level and the heating power. Up to the critical density, most of the plasma parameters change slowly with increasing density. A further increase of n_e results in a rather abrupt change of the turbulence–induced radial particle flux $\tilde{\Gamma}$ by a factor of 2. Since the local density n drops with detachment the strong rise of $\tilde{\Gamma}$ manifests in an increase of the effective radial drift velocity caused by turbulence. Although the fluctuation level of E_p and n decreases only slightly, the turbulence–induced flux shows a considerable increase. This is due to a significant increase of the correlation of turbulence in the detached state. The increase of the cross–correlation function of the fluctuations by a factor of 2 as picked up from two poloidally spaced probes indicates a rise of the turbulent mixing length (i.e. the size of the turbulent cells). The qualitative difference of the properties of edge turbulence between detached and non–detached plasmas are also evident from the frequency and wave number spectra (Fig.18). The mean value

of the k–spectra is shifted towards much longer wave lengths with detachment. These changes of the edge turbulence cause a significant reduction of the phase velocity in poloidal direction, thereby indicating a reduction of the poloidal plasma rotation. In a detached plasma the rotation velocity reduces almost to zero, the floating potential and the radial electric field are reduced significantly as well. Fig. 19 shows the radial profiles of plasma parameters during the detachment.
We observe that in the detached state the radial transport is large. This finding can be due to the fact that the shear of the poloidal rotation velocity is small in this case. As the size of the turbulent cells is inversely proportional to the square root of the shear, the cells become large thereby increasing the transport [31].

3.4 Limiter biasing

Preliminary measurements have been made using the multi–tip probe in ohmic discharges with negative biasing of the ALT–II limiter. Radial profiles of the time averaged floating potential U_f and poloidal electric field E_p are plotted in Fig. 21. In this series of discharges, the ALT–II toroidal belt was biased -180 V with respect to the liner. Six of eight segments of the belt limiter were positioned as the main limiter at 44.0 cm, while the remaining 2 segments, blades 4 and 8, were shorted to the TEXTOR vessel and retracted to 48.0 cm. The presence of the grounded blades at 48.0 cm is clearly seen in the floating potential profile, as is the presence of the biased belt. This structure has been independently measured with the fast reciprocating probe (Fig. 22a), and demonstrates that the radial potential profile can be controlled through configuration of the ALT–II toroidal belt [34].
The radial profile of the time–averaged poloidal electric field E_p (Fig. 21b) indicates that poloidal electric fields approaching 100 V/cm and enhanced over ohmic values, are generated in the scrape–off layer during limiter biasing. The associated convective particle flux is radially outward in the region from 43 to 48 cm. In the region between 46 and 48 cm, E_p and the corresponding particle flux approach zero. Comparison with scrape–off layer density profiles from similar discharges in the same series (Fig. 22b) for both unbiased and ±350 V biased ohmic discharges, reveals that the radial density profile steepens in the region where E_p and the associated outward particle

flux approach zero, although the steepening of the density gradient is likely also due in large part to the steep radial potential well and radial electric field in the region between 44 cm and 45 cm. Apparently both features of the D.C. electric fields contribute to the formation of the steep density gradient ("pedestal") in the SOL during ALT–II biasing.
To date, no extensive measurements of the characteristics of the electrostatic fluctuations during limiter biasing have been performed, although it might be possible to influence the level of such fluctuations through the application of limiter biasing [35, 36].

4 CONCLUSIONS AND FUTURE PLANS

The multi–electrode probe demonstrated to be an efficient tool for experimental study of the boundary plasma parameters. A large amount of information (up to 14 different quantities simultaneously) characterizing the plasma boundary, allow a detailed investigation of cross–field transport. The design of the probes allowed measurements in the SOL as well as inside the separatrix, even in discharges with auxiliary heating.
The investigations of regimes with different transport in the plasma boundary (e.g. detached plasma) demonstrated significant changes in the structure of electric fields in the TEXTOR boundary, accompanied by modifications in poloidal plasma rotation and $E \times B$ particle transport. The observed sensitivity of the turbulence–driven cross–field particle transport to changes in the plasma boundary properties indicates their relevance to the correlative properties of edge turbulence. The transport in the boundary due to turbulence seems to be linked to poloidal plasma rotation. In particular, the transition to the detached plasma state was found to be due to a significant decrease of the poloidal plasma rotation and a profound change of the characteristics of edge turbulence.
Further improvement of both the design of the multi electrode probe and of the measuring technique may increase the experimental capability of the probes. Two additional tips implemented could simultaneously provide data on toroidal plasma flow, enabling 3–D analysis of transport processes in the plasma boundary.
The development of a novel experimental technique for the measurement of

electron temperature fluctuations would allow the investigation of both, convective and conductive transport due to edge turbulence. The design of the probes fulfills the requirements for such measurements.
In future studies we may also concentrate on effects of auxiliary heating on turbulence–driven transport. In view of the comprehensive plasma boundary diagnostics available on TEXTOR, a combination of the probe measurements with other diagnostics may result in new aspects of anomalous transport research.

ACKNOWLEDGEMENTS

The authors would like to thank Prof. E. Hintz, Dr. J. Schlueter, Prof. P. Vandenplas and Prof. G. Wolf for their constant interest and support of this work and for creating an atmosphere of creative international cooperation. The authors are indebted to A. Cosler, A. Charl and J. Neander for their contribution to the development and improvement of the probe system. Special thanks are due to the operating team of TEXTOR for providing a reliably functioning tokamak. Many thanks to Dr. B. Schweer for providing valuable data.

References

[1] P. Bogen and E. Hintz in Physics of Plasma–Wall interactions in Controlled Fusion, Plenum ress, New York, 1986, eds. D. E. Post and R. Behrisch.

[2] U. Samm, P. Bogen, H. Hartwig et al., J. Nucl. Mat., 162–164, 24, (1988).

[3] A. Pospieszczyk, F. Anmayer, H. L. Bay et al., J. Nucl. Mat., 162–164, 574, (1988).

[4] P. S. Liewer, Nucl. Fusion, 25, 543, (1985)

[5] A. J. Wootton, Austin Report DOE/ER/53267 FRCR #371, (1990) to appear in J. Nucl. Mat. 176–177 (1990).

[6] A. Komori, S. Masamune, O. Mutarai et al., J. Nucl. Mat., 162–164, 231, (1988).

[7] J. Winter, to appear in J. Nucl. Mat. 176–177 (1990).

[8] S. J. Zweben, P. C. Liewer, R. W. Gould, J. Nucl. Materials, 111–112, 39, (1982).

[9] A. S. Wan, T. F. Yang, R. R. Parker, Bull. Amer. Soc., 29, 1223, (1984).

[10] P. Staib, J. Nucl. Materials, 111–112, 109, (1982).

[11] K. Höthker, W. Bieger, H. J. Belitz, 16th European Conf. on Contr. Fusion and Plasma Physics, Venice, 13B, 1525, (1989).

[12] G. Fuchs, B. Schlarbaum et al., J. Nucl. Material, 145–147, 268, (1987).

[13] W. O. Hofer, KFA report no. 2317, 6, (1990).

[14] G. Fuchs and A. Nicolai, Nucl. Fusion, 20, 1247, (1980).

[15] S. K. Erents, G. M. McCracken, J. A. Tagle et al., Nucl. Fusion, 26, 1591, (1986).

[16] A. V. Nedospasov, V. G. Petrov, G. N. Fieldman, Nucl. Fusion, 25, 21, (1985).

[17] A. V. Nedospasov, S. S. Bychkov, et al., to appear in J. Nucl. Mat., 176–177 (1990).

[18] F. Chen, Electric probes in Plasma diagnostics, edt. by R. Huddlestone and S. Leonard, Mir, Moscow, 149, (1967) (in Russian).

[19] V. N. Budnikov, G. V. Gerasimenko, L. A. Esipov et al., Sov. J. Tech. Phys. 57, 393, (1987).

[20] V. A. Godjak, A. N. Ivanov, A. A. Kuzovnikov, Sov. J. Tech. Phys. 37, 1067, (1966) (in Russian).

[21] B. I. Kanaev, V. V. Pitersky, E. E. Jushmanov, Sov. J. Tech. Phys. 44, 2302, (1974) (in Russian).

[22] L. Bogomolov, A. Chernilevsky, USSR annual conference on Plasma Physics and Fusion, Zvenigorod, USSR, (1990).

[23] K. W. Gentle, Univ. of Texas, Austin, Report DOE/ET-5343-11, ERCR #266, 16, (1984).

[24] R. A. Moyer, R. Van Nieuwenhove, G. Van Oost, D. Bora et al., to appear in J. Nucl. Mat. , 176–177 (1990)

[25] Ch. P. Ritz, R. D. Bengston, S. J. Levinson et al., Phys. of Fluids 27, 2956, (1984).

[26] R. Van Nieuwenhove and G. Van Oost, Fusion Engineering and Design 12, 231 (1990)

[27] K. Höthker et al., Proc. 17_{th} Eur. Conf. on Controlled Fusion and Plasma Physics, Amsterdam, 14B, 1568 (1990).

[28] V. P. Budaev, L. M. Bogomolov, B. V. Borovsky et al., J. Nucl. Mat. , 176–177 (1990)

[29] R. Van Nieuwenhove and G. Van Oost., Submitted to Plasma Physics and Controlled Fusion

[30] U. Samm et al., Report KFA Jülich Jül-2123, 1987.

[31] Ch. Ritz, H. Lin, R.D. Bengston et al., Proc. 17th European Conf. on Contr. Fusion and Plasma Physics, Amsterdam, 14B, 1456 (1990).

[32] D.E. Smith, E.J. Powers and G.S. Caldwell, IEEE Transactions of Plasma Science, Vol. PS–2, 261 (1974)

[33] H. Amemiya and G. Fuchs, Report to appear.

[34] R. Doerner, R.W. Conn, D. Gray, et al., Bull. American Phys. Soc., 35, 1988 (1990).

[35] K.C. Shaing and E.C. Crume, Jr., Phys. Rev. Lett. 63, 2369 (1989).

[36] R. Lehmer, L. Schmitz, G. Tynan, et al., Bull. American Phys. Soc., 35, 1947 (1990).

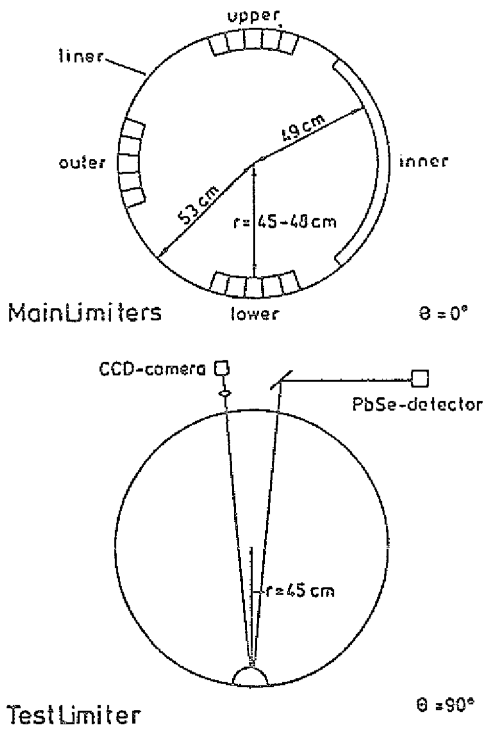

Fig.1 Schematic view of the poloidal cross section showing the main limiter positions.

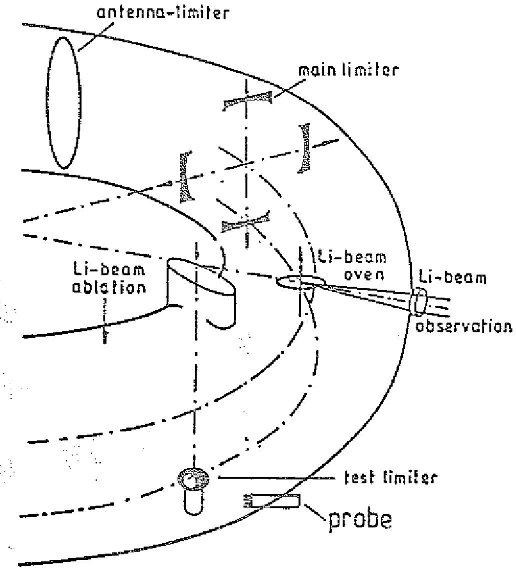

Fig.2 Schematic drawing showing the position of the main and the reference (test) limiters.

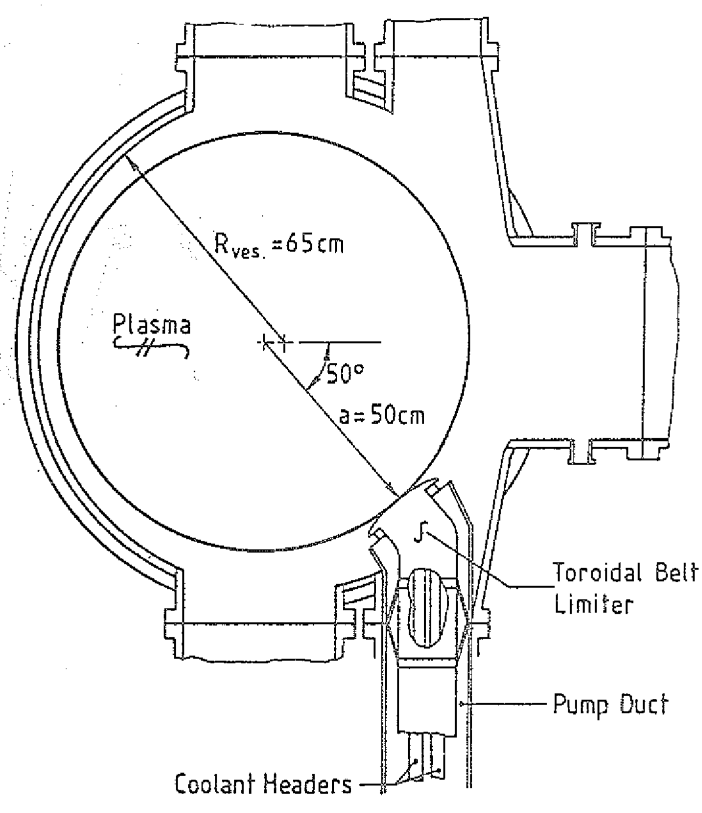

Fig.3 Schematic view showing the position of the ALT–II limiter.

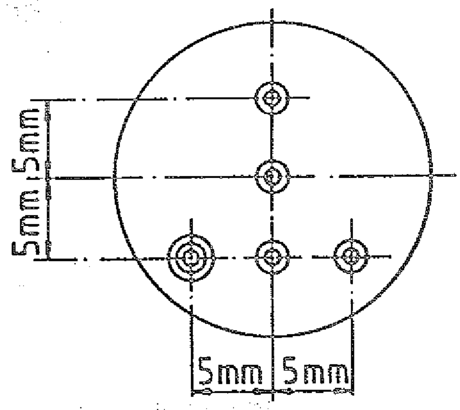

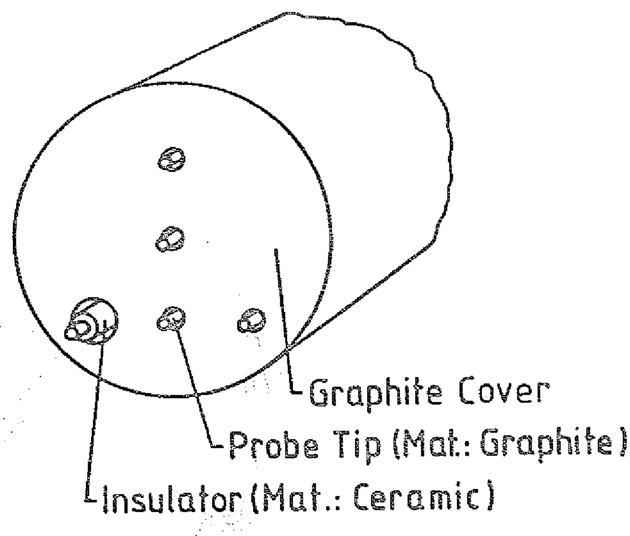

Fig.4 Langmuir multi-electrode arrangement.

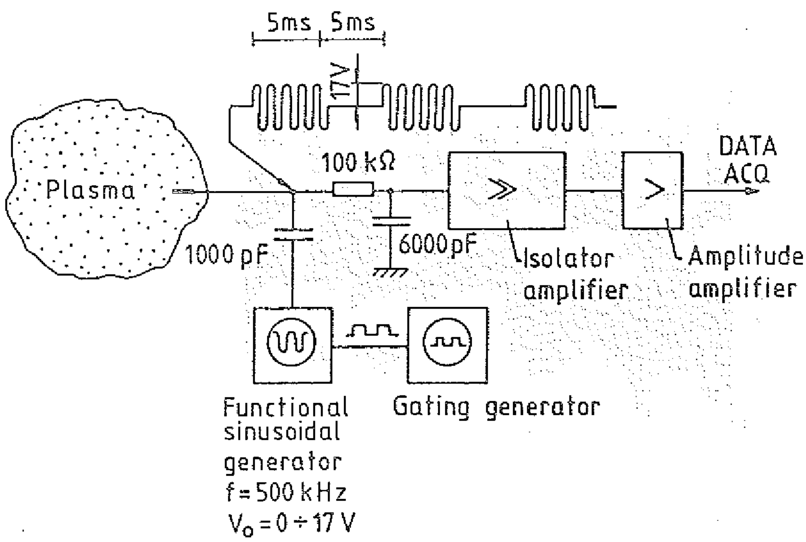

Fig.5 Schematic diagram of the electric circuit used in the oscillatory probe technique for T_e measurement.

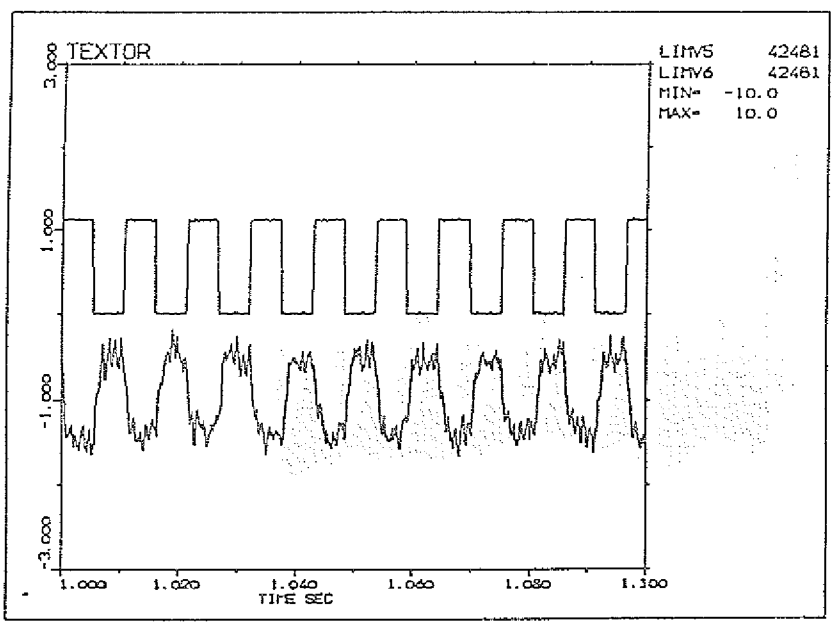

Fig.6 Typical floating potential picked up from the probe with a harmonic disturbance applied which allows to evaluate electron temperature. The upper curve shows the gating pulses.

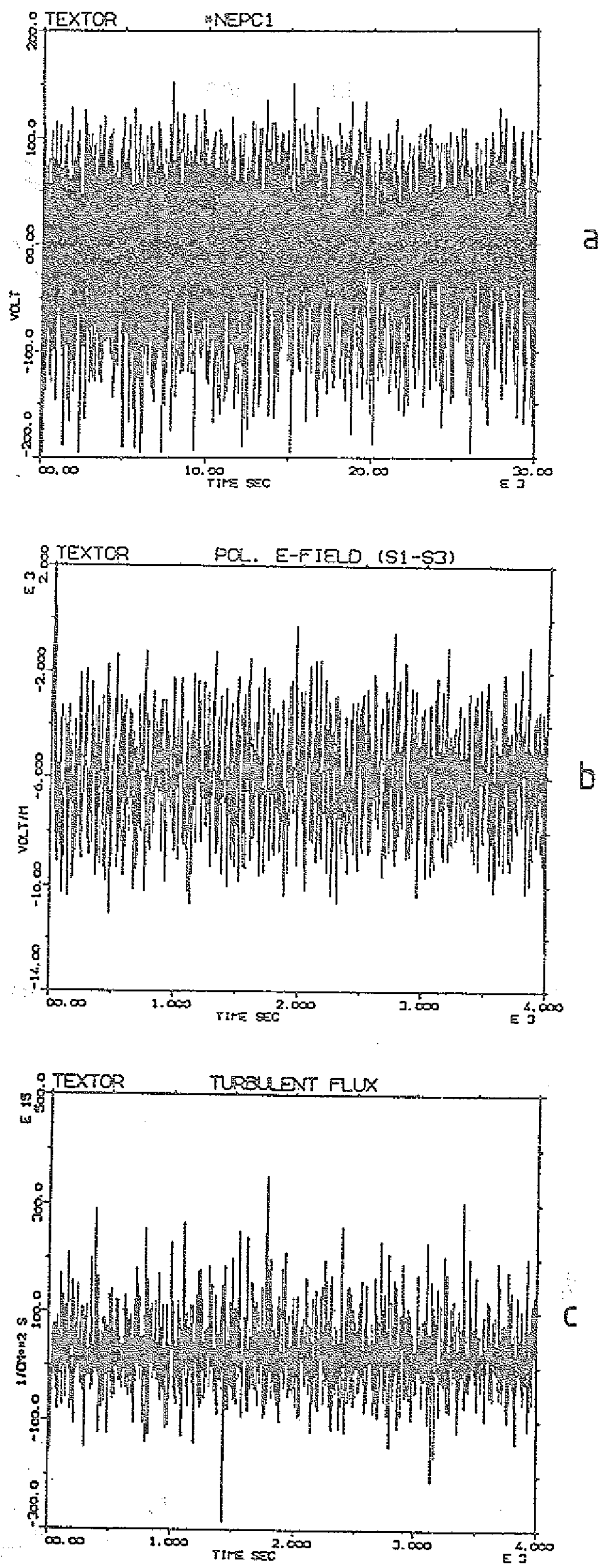

Fig.7 Typical probe signal in ohmically heated discharges.
a) Ion saturation current, b) Poloidal electric field, c) Turbulence induced particle flux.

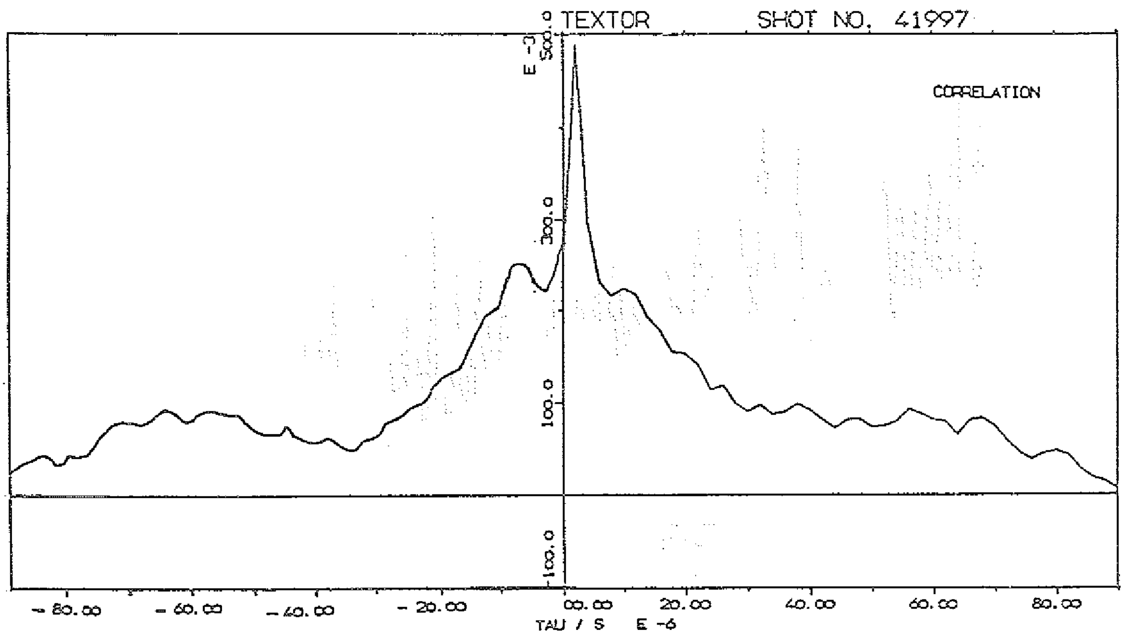

Fig.8 Typical example of the cross–correlation function of the ion saturation current and poloidal electric field fluctuations.

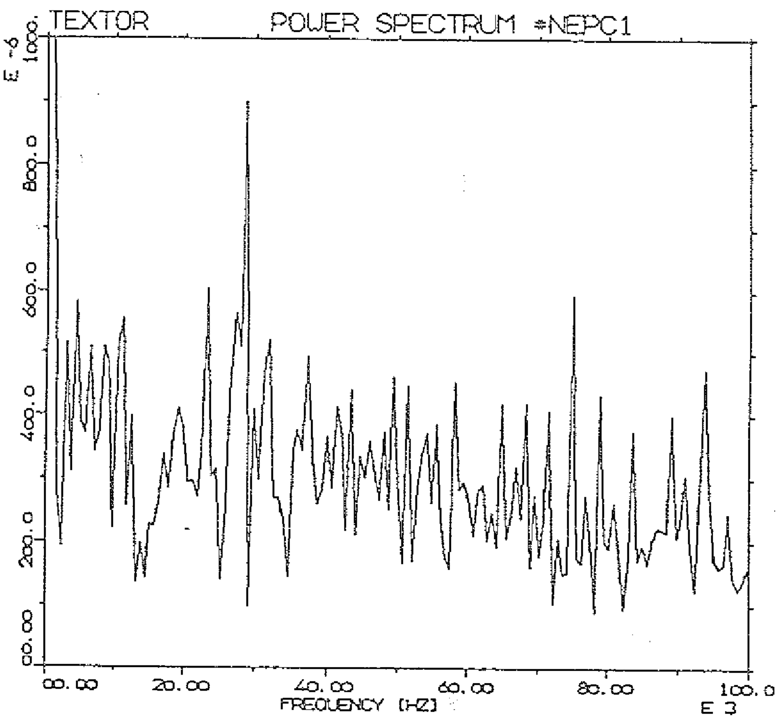

a

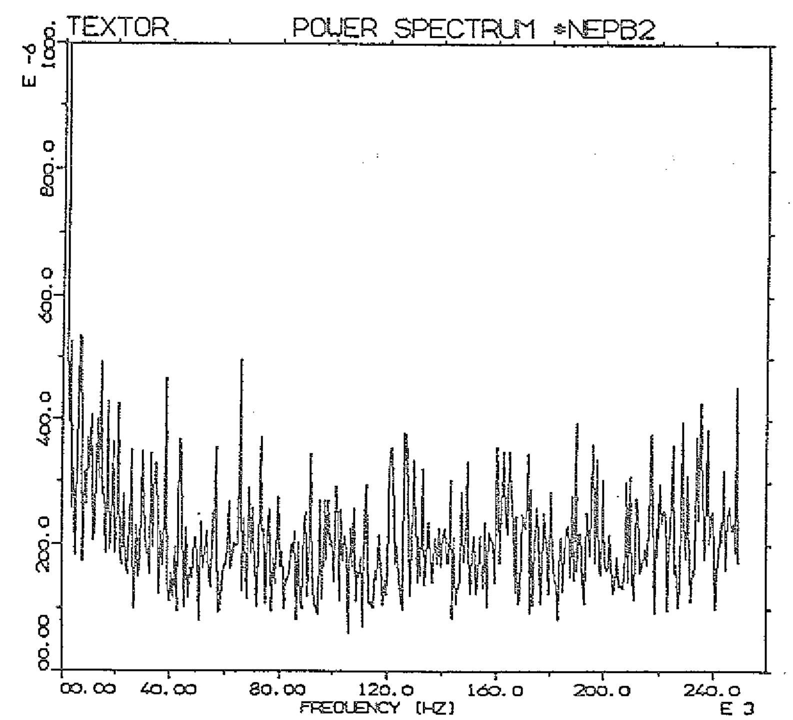

b

Fig.9 Frequency spectra of a) floating potential b) and density fluctuations. (#41703).

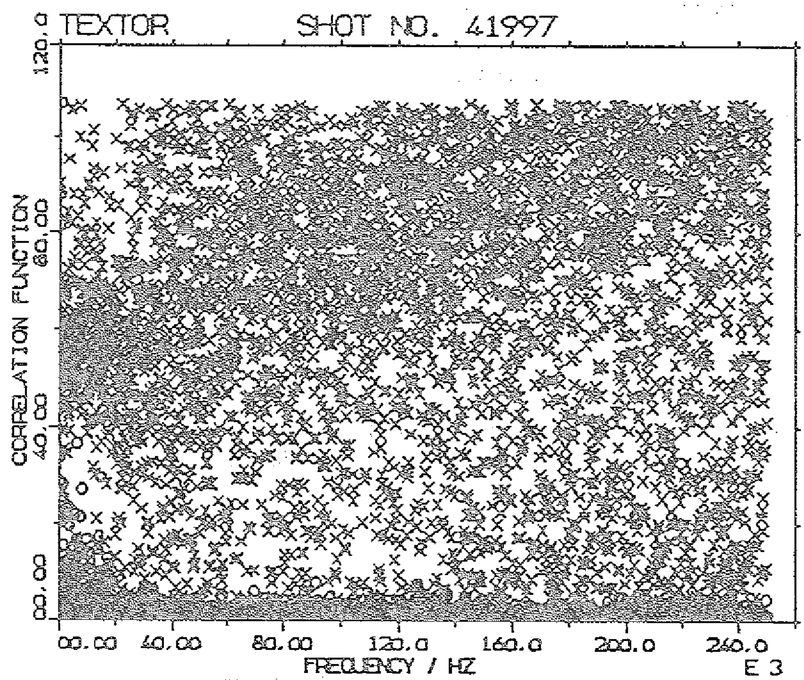

Fig.10 Examples of the statistical dispersion relation obtained, using the fluctuations of floating potentials picked up from a pair of poloidally spaced probes.

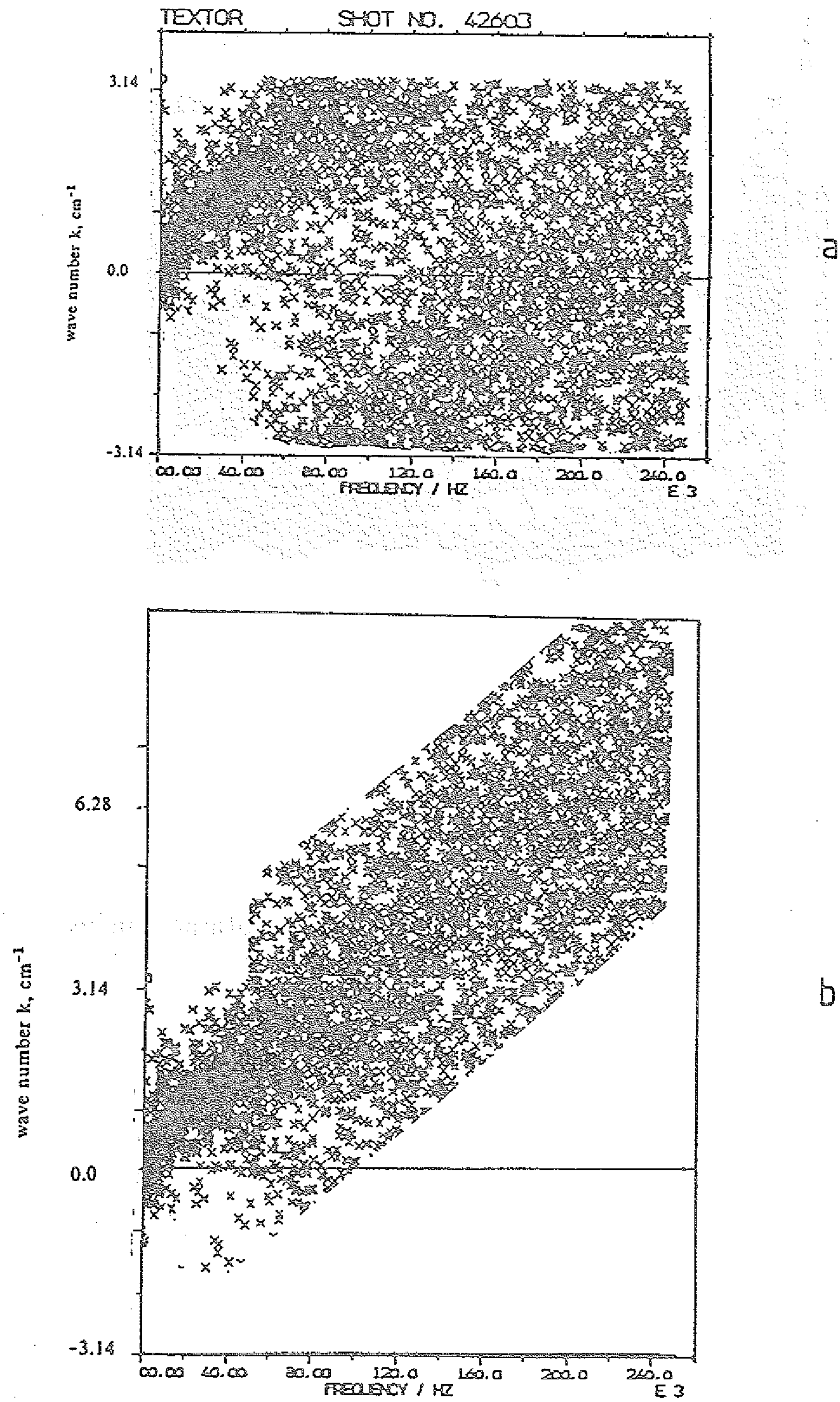

Fig.11 A statistical dispersion relation in the case of short-wave aliasing (a). A corrected plot of the statistical dispersion relation (b).

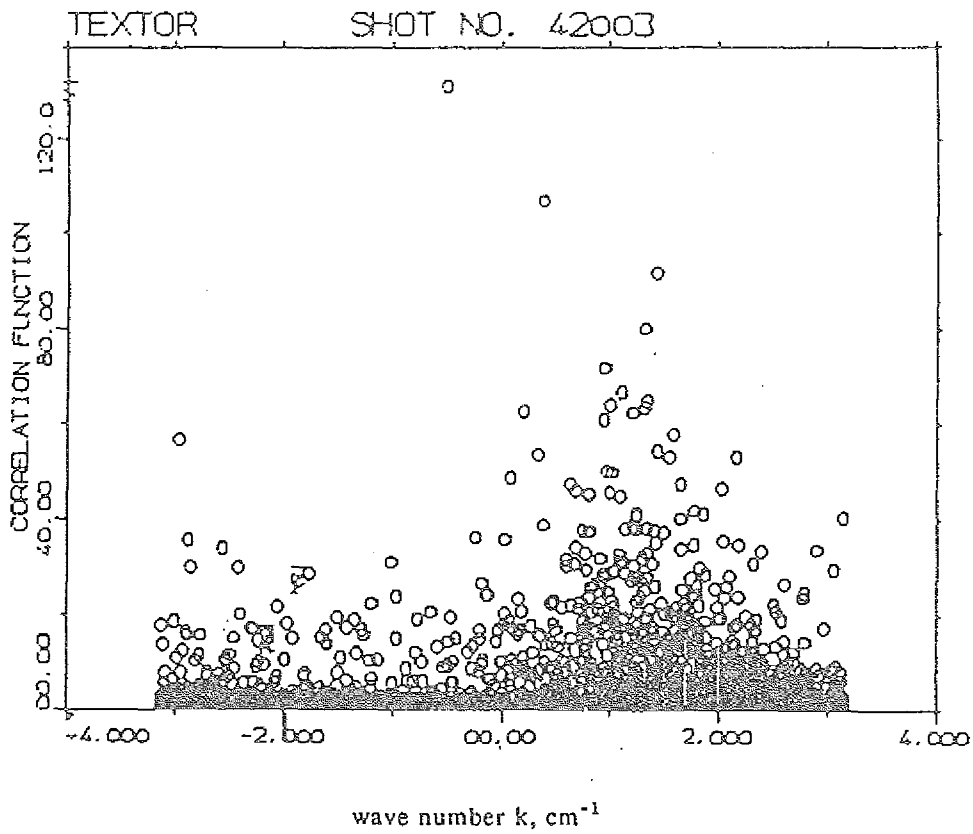

Fig.12 Example of the frequency integrated k–spectrum of the floating potential fluctuations.

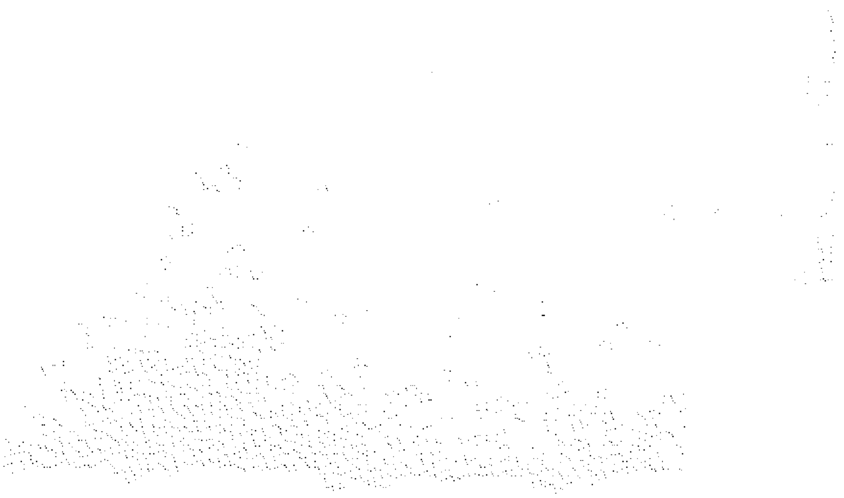

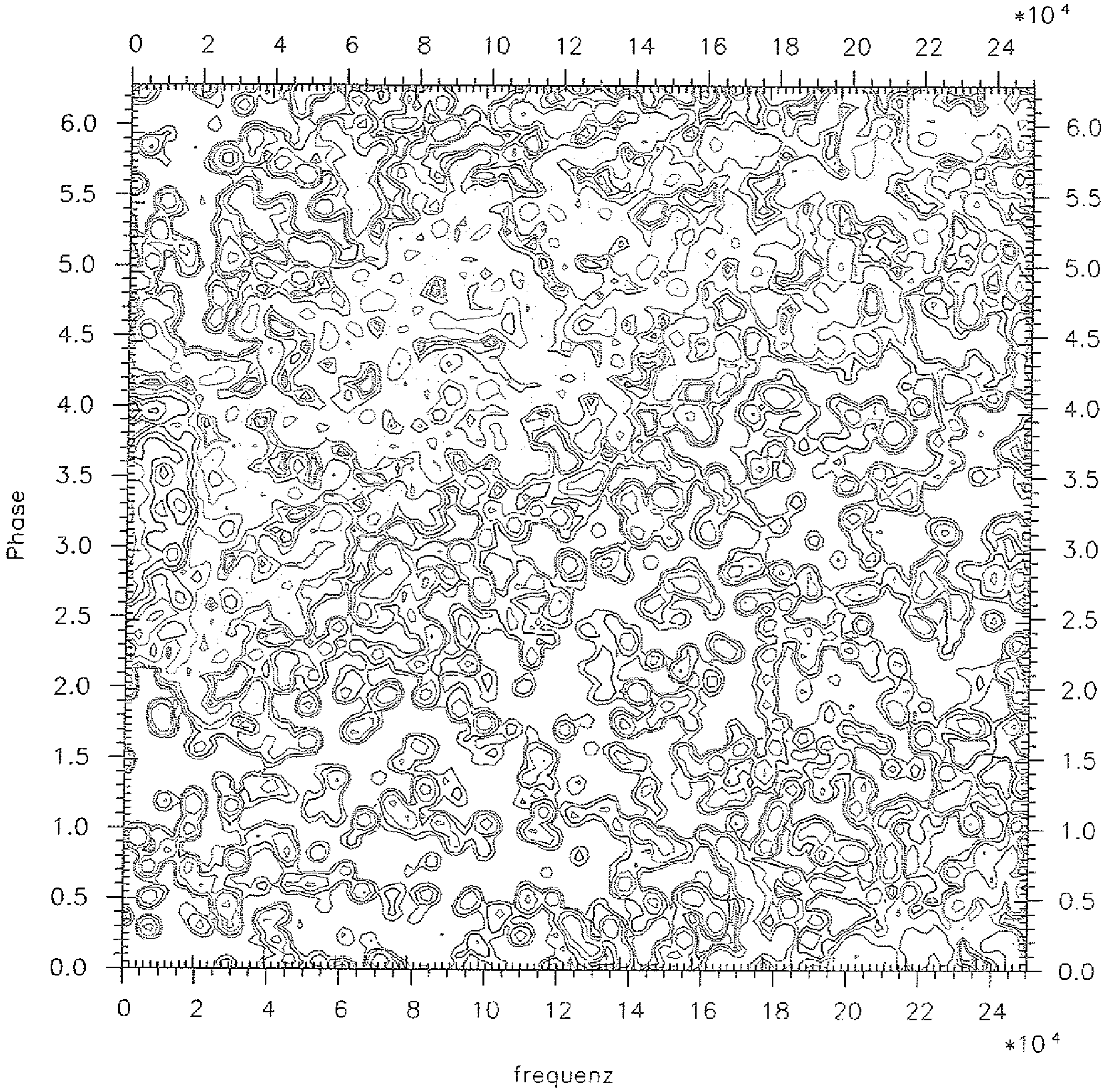

Fig.13 Contour plot of the statistical $S(k,w)$–function for floating potential fluctuations picked up from a pair of poloidally spaced probes (#42003).

WERT STRICH

0.3882
0.66
1.122
1.9073
3.2425
5.5122
9.3708
15.9303
27.0815
46.0385
78.2655
133.051

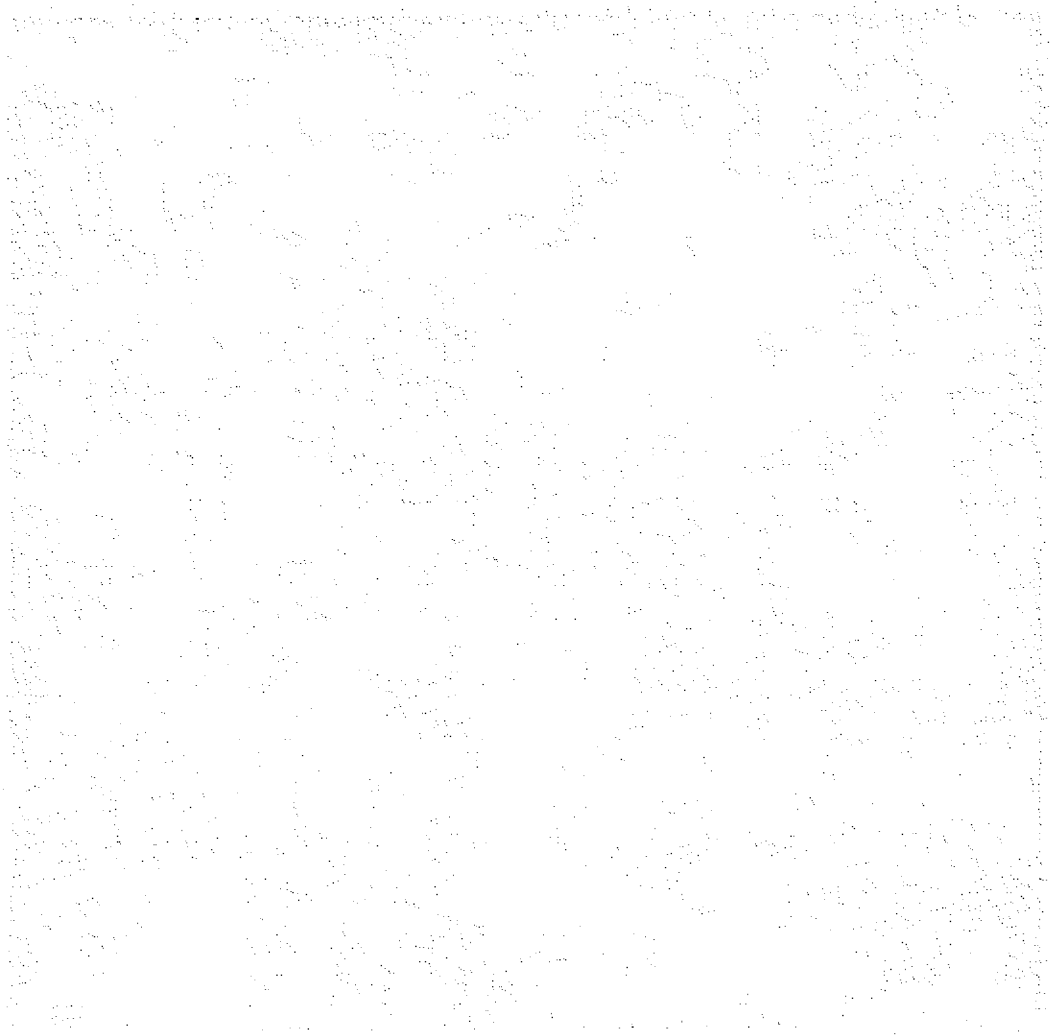

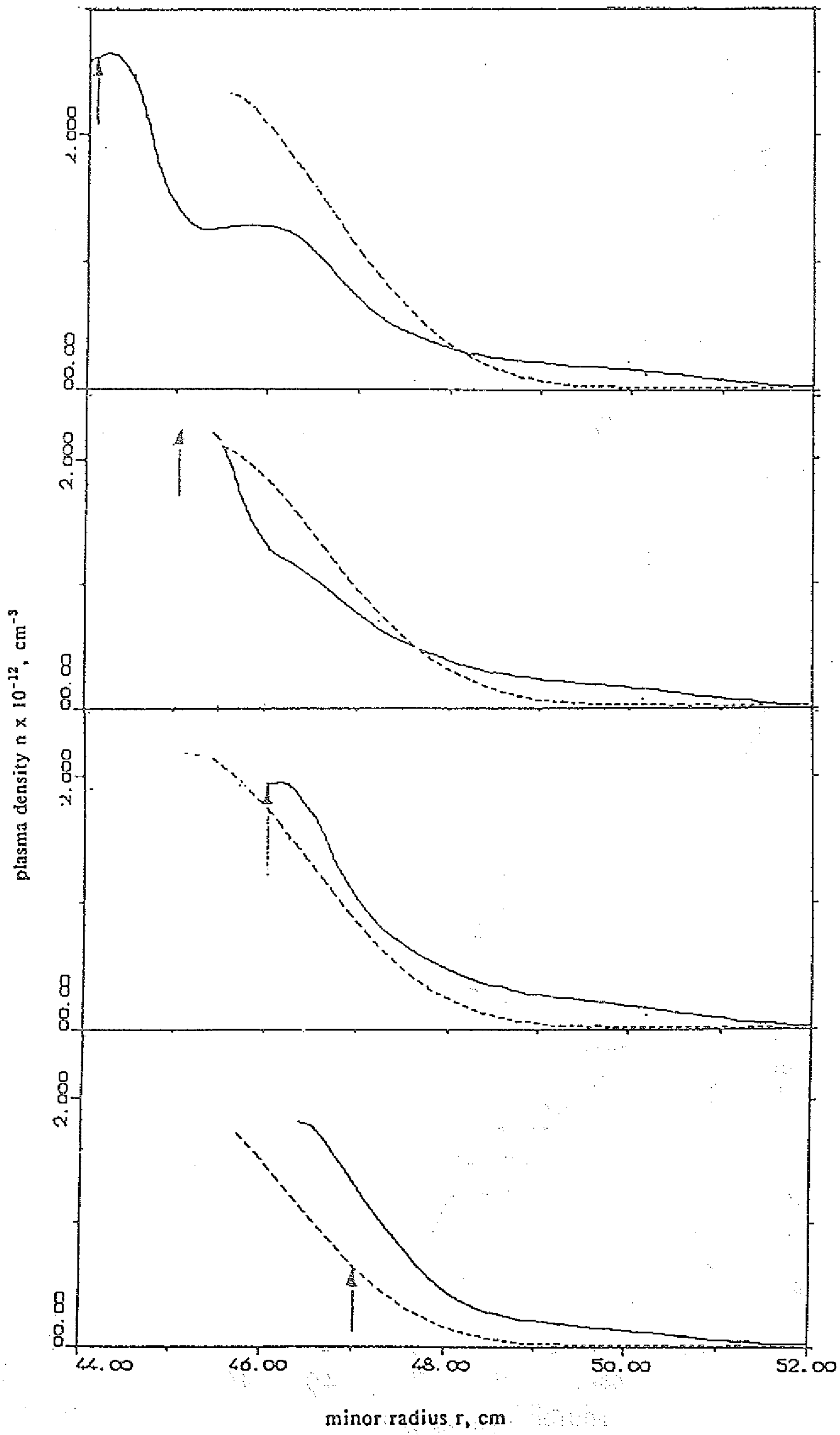

Fig.14 Radial profiles of the plasma density being disturbed by the insertion of the probes
a) $r_p = 44$ cm, b)$r_p = 45$ cm, c)$r_p = 46$ cm, d)$r_p = 47$ cm.
(#41680, #41681, #41682, #41683).

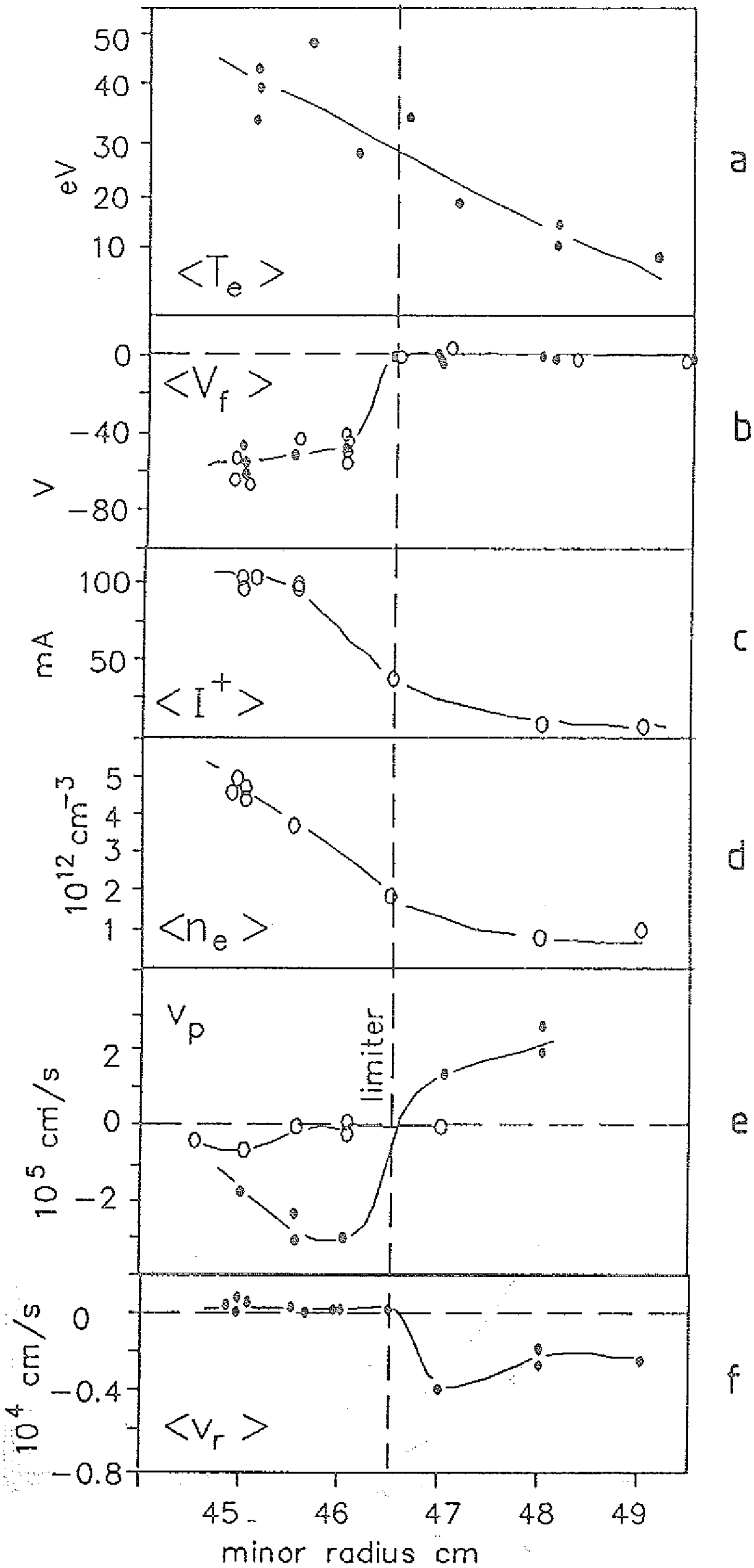

Fig.15 Radial profiles of the boundary plasma parameters in ohmically heated plasmas
a) Electron temperature T_e, b) Floating potential V_f, c) Ion saturation current I^+,
d) Local lasma density n_e, e) Poloidal phase velocity v_p, f) Radial phase velocity v_r,

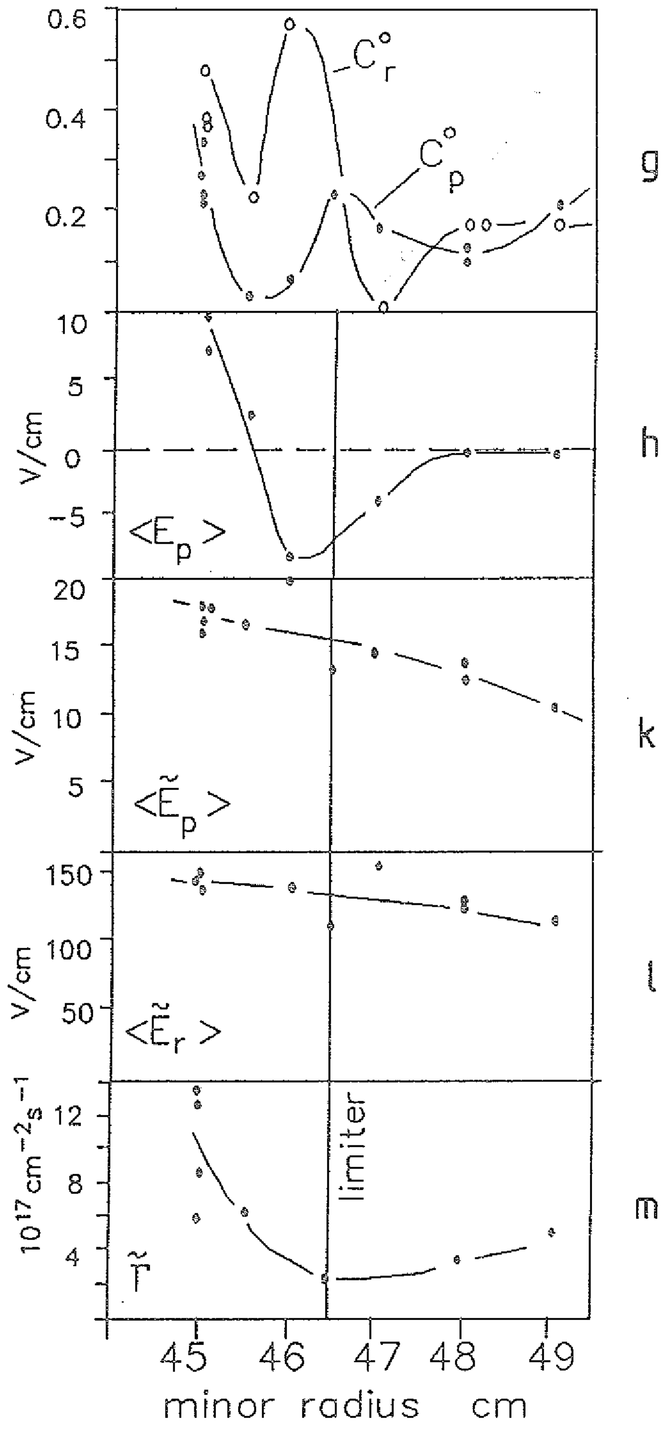

Fig.15 (continuation) g) Zero cross-correlation C_p^0 and C_r^0 for floating potential fluctuations on a pair of poloidally and radially seperated probes, h) DC poloidal electric field E_p, k) RMS of poloidal electric field $\tilde{E}_p$, l) RMS of radial electric field $\tilde{E}_r$, m) Turbulence driven particle flux $\tilde{\Gamma}$ (#41699–41710). $n_e = 3 \times 10^{13}\text{cm}^{-3}$, $I_p = 340kA$.

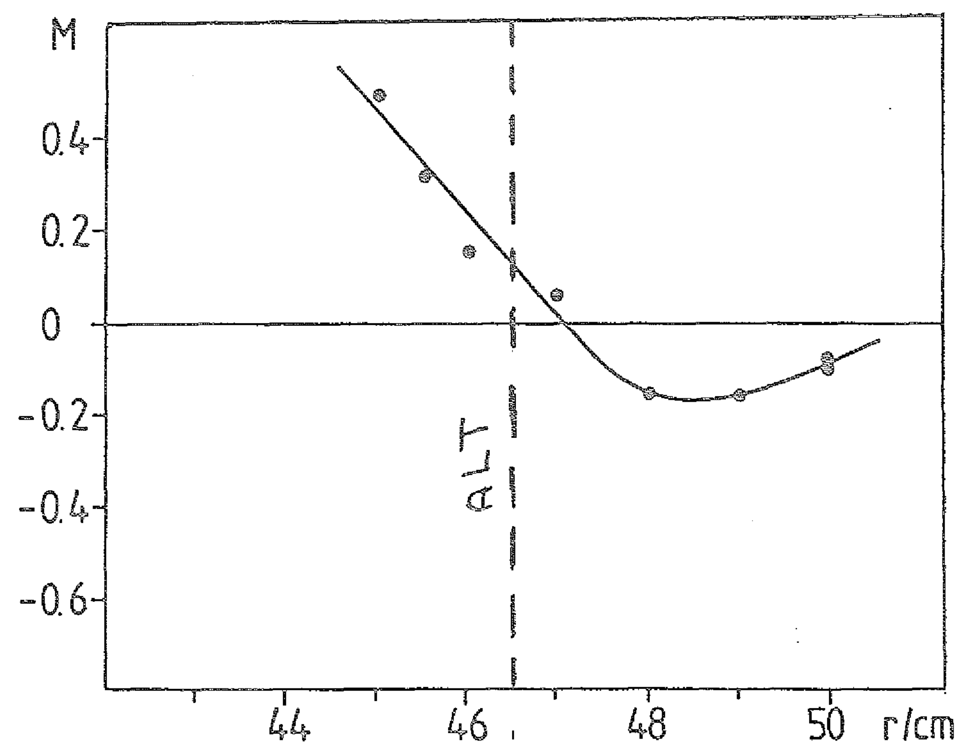

Fig.16 Mach number of the plasma flow parallel to the magnetic field as a function of minor radius. The positive direction coincides with that of the plasma current.

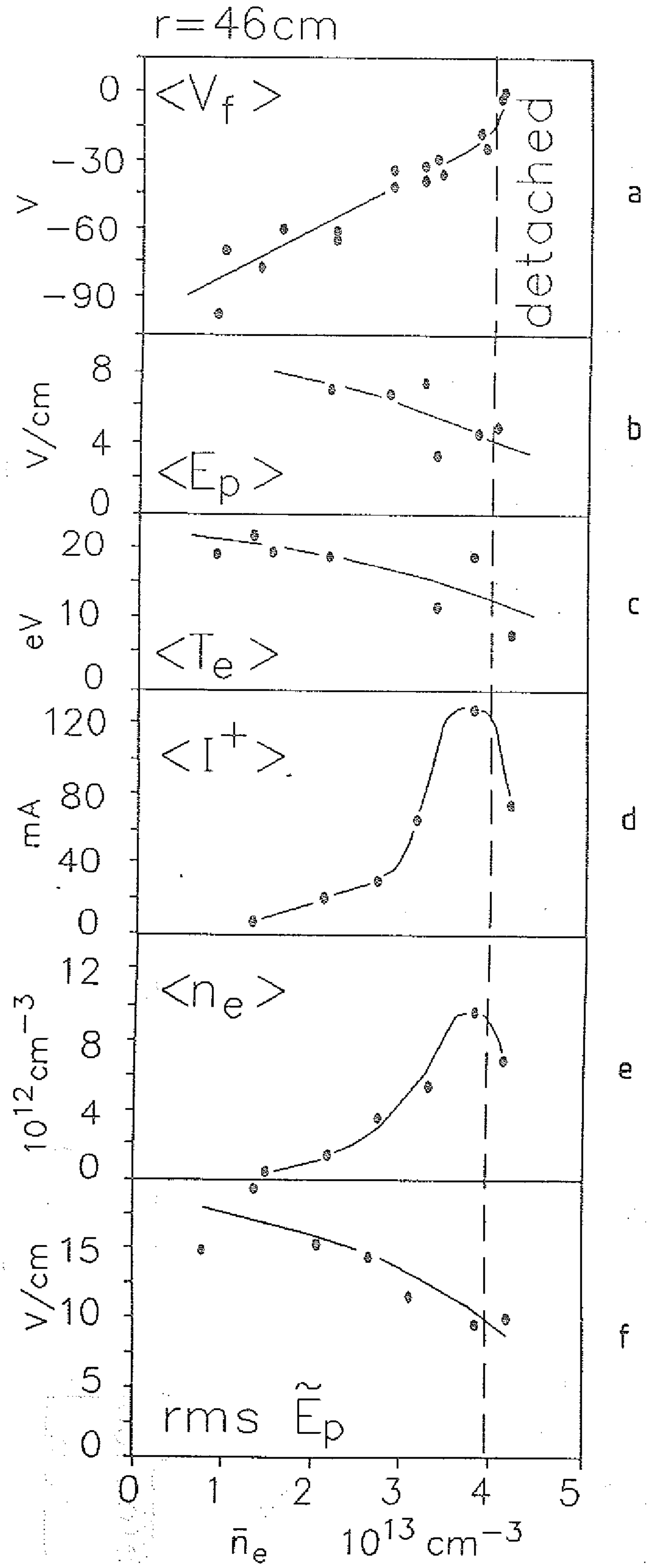

Fig.17 Edge plasma parameter as a function of the line averaged density. The specification of symbols is similar to that described in Fig.15. The probes were fixed at $r_p = 46$ cm (#41685–41698).

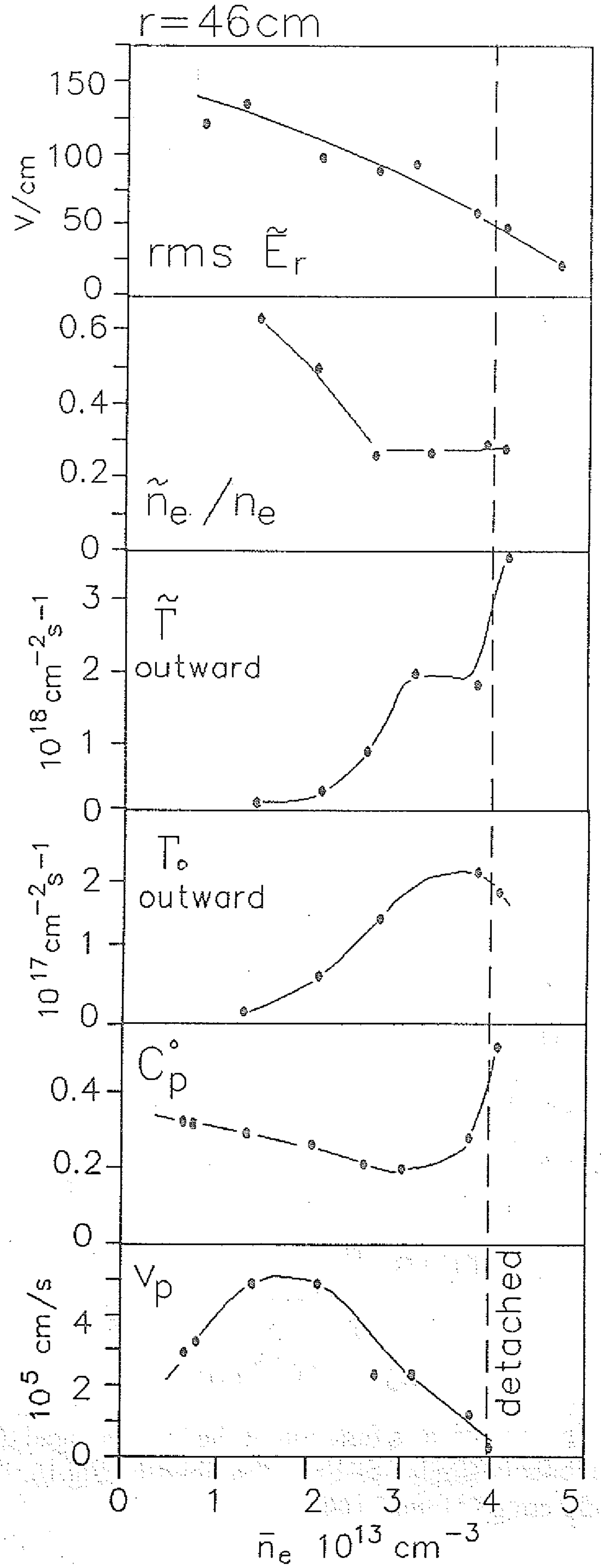
r=46cm
V/cm
150
100
50
0
rms $\tilde{E}_r$
g
0.6
0.4
0.2
0
$\tilde{n}_e / n_e$
h
10^{18} cm^{-2}s^{-1}
3
2
1
0
$\tilde{\Gamma}$ outward
i
10^{17} cm^{-2}s^{-1}
2
1
0
Γ_o outward
j
0.4
0.2
0
C_p^o
k
10^5 cm/s
4
2
0
V_p
detached
l
0
1
2
3
4
5
$\bar{n}_e$ 10^{13} cm^{-3}

Fig.17 .

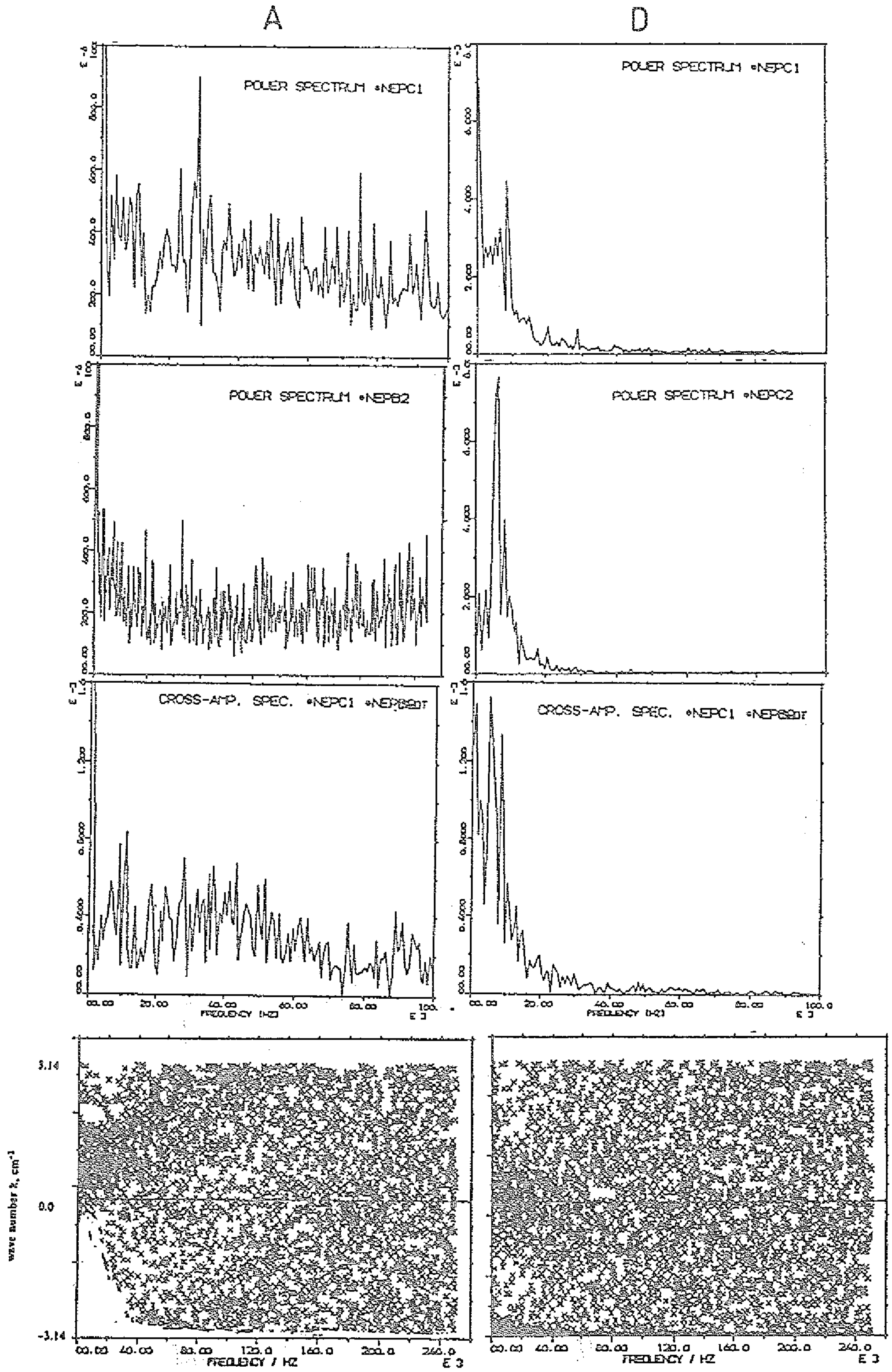

Fig.18 An evolution of fluctuation spectra during the transition to plasma detachment. (A– left, D– right)
a) Power spectrum of density fluctuation, b) Power spectrum of floating potential, c) Cross power spectrum of density and floating potential, d) statistical dispersion relation.
The probes were fixed at $r_p = 46$ cm. (#41703 and #41680).

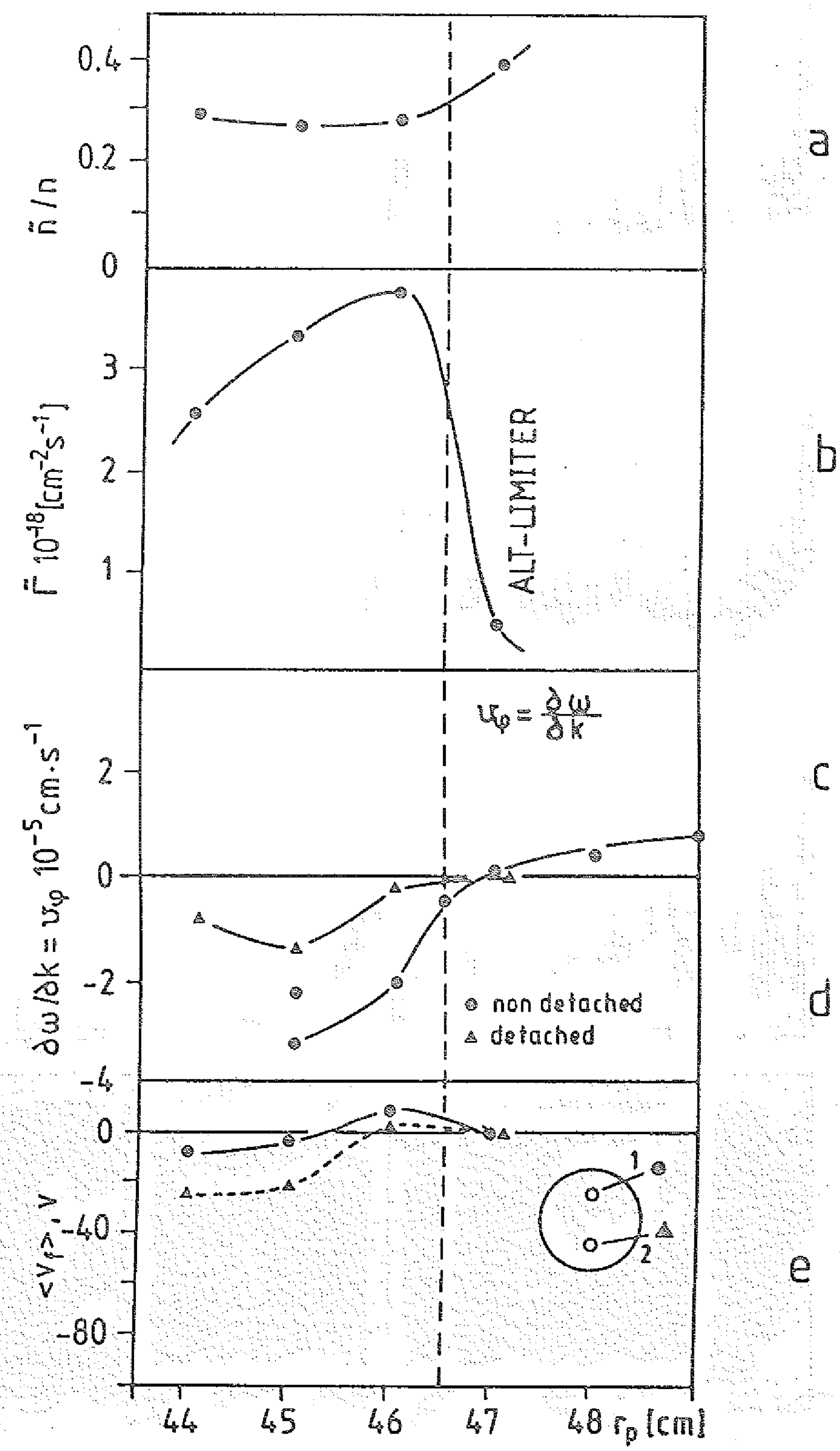

Fig.19 Radial profiles of plasma parameters during the detachment. Symbols are same as in Fig.15 (#41680–#41683).

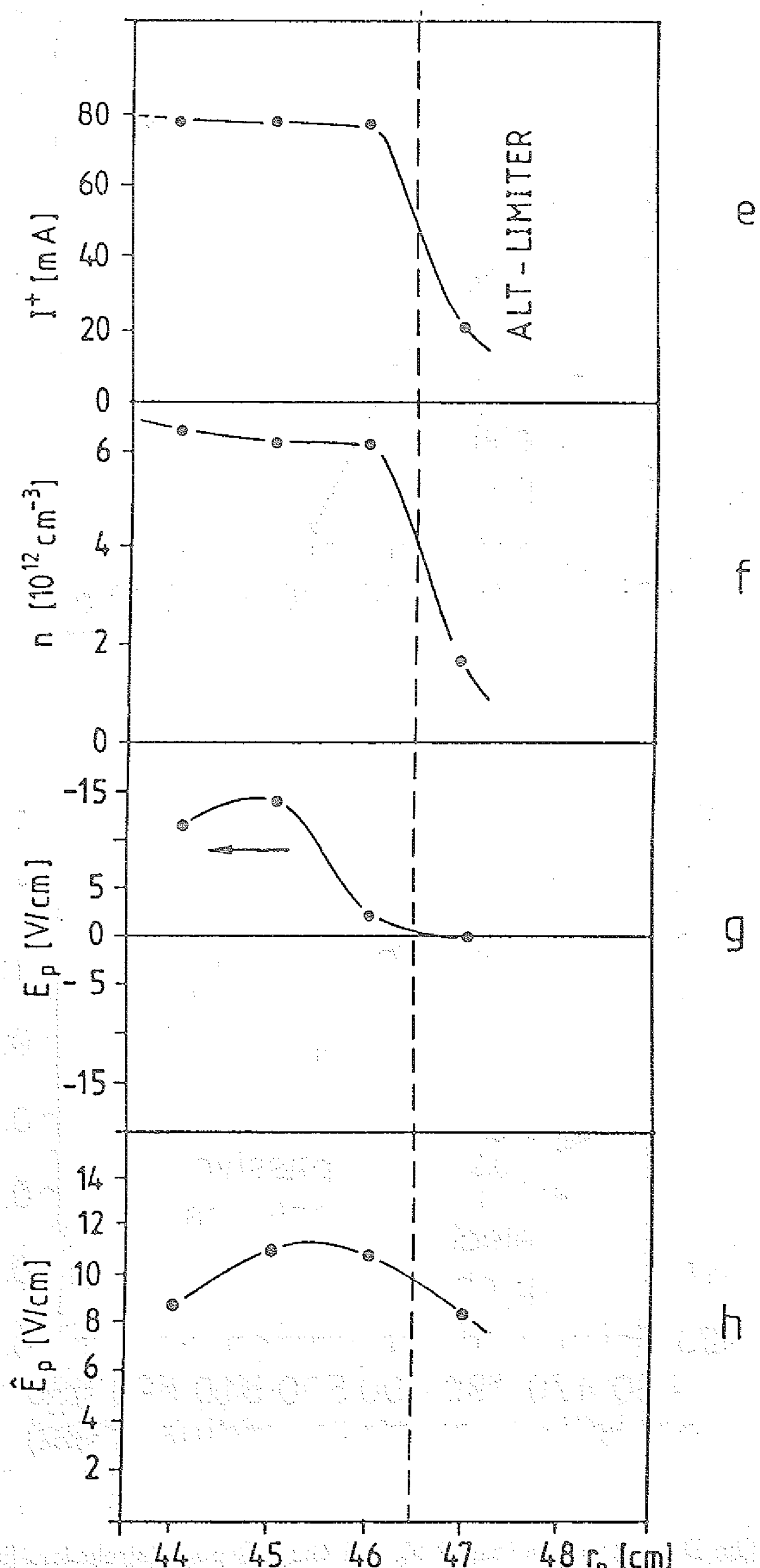

Fig.19 continuation

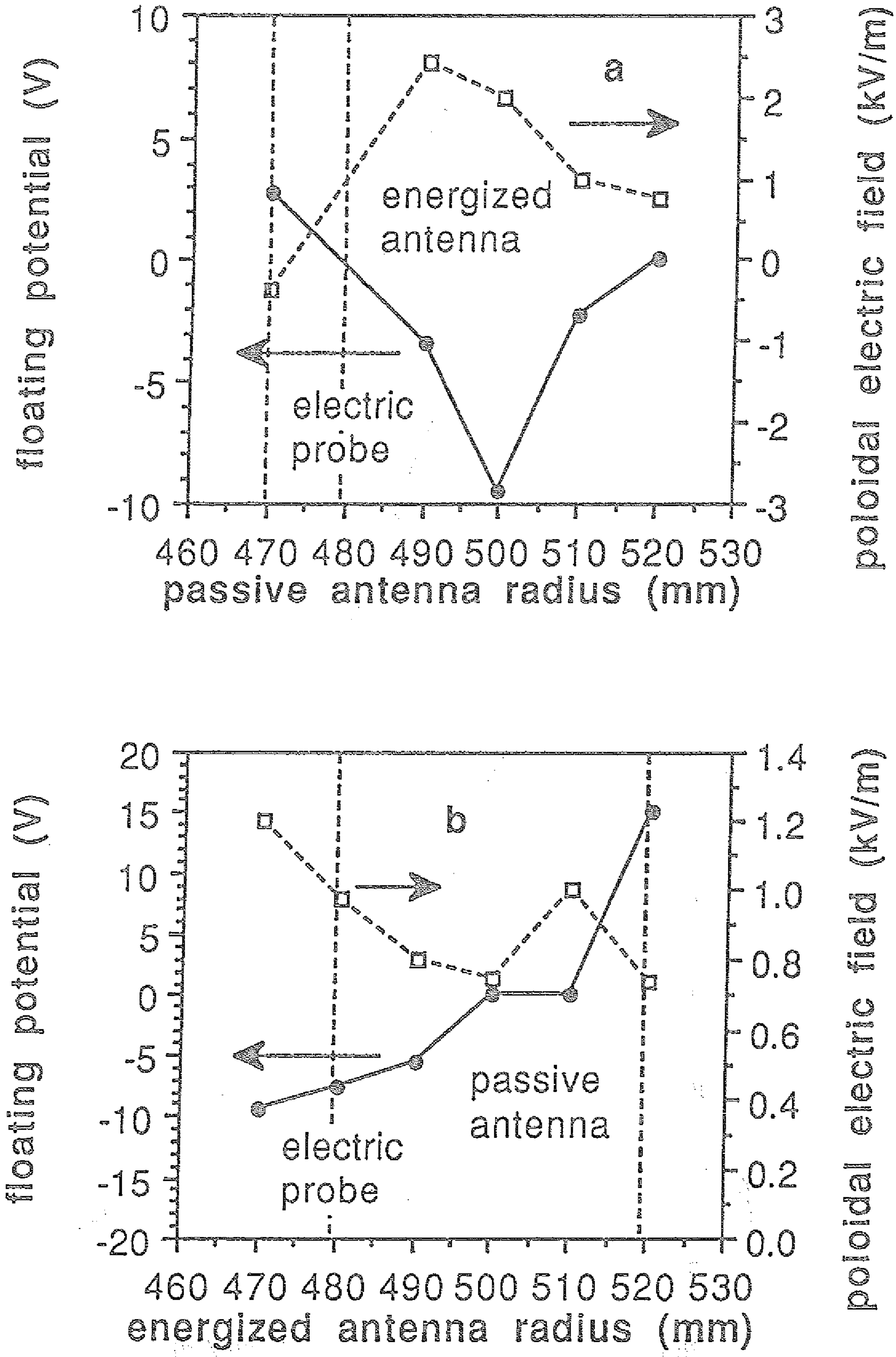

Fig.20 The DC floating potential V_f and the DC poloidal electric field E_p as functions of the passive a) and excited b) antenna positions (#41816–21, #41824–29).

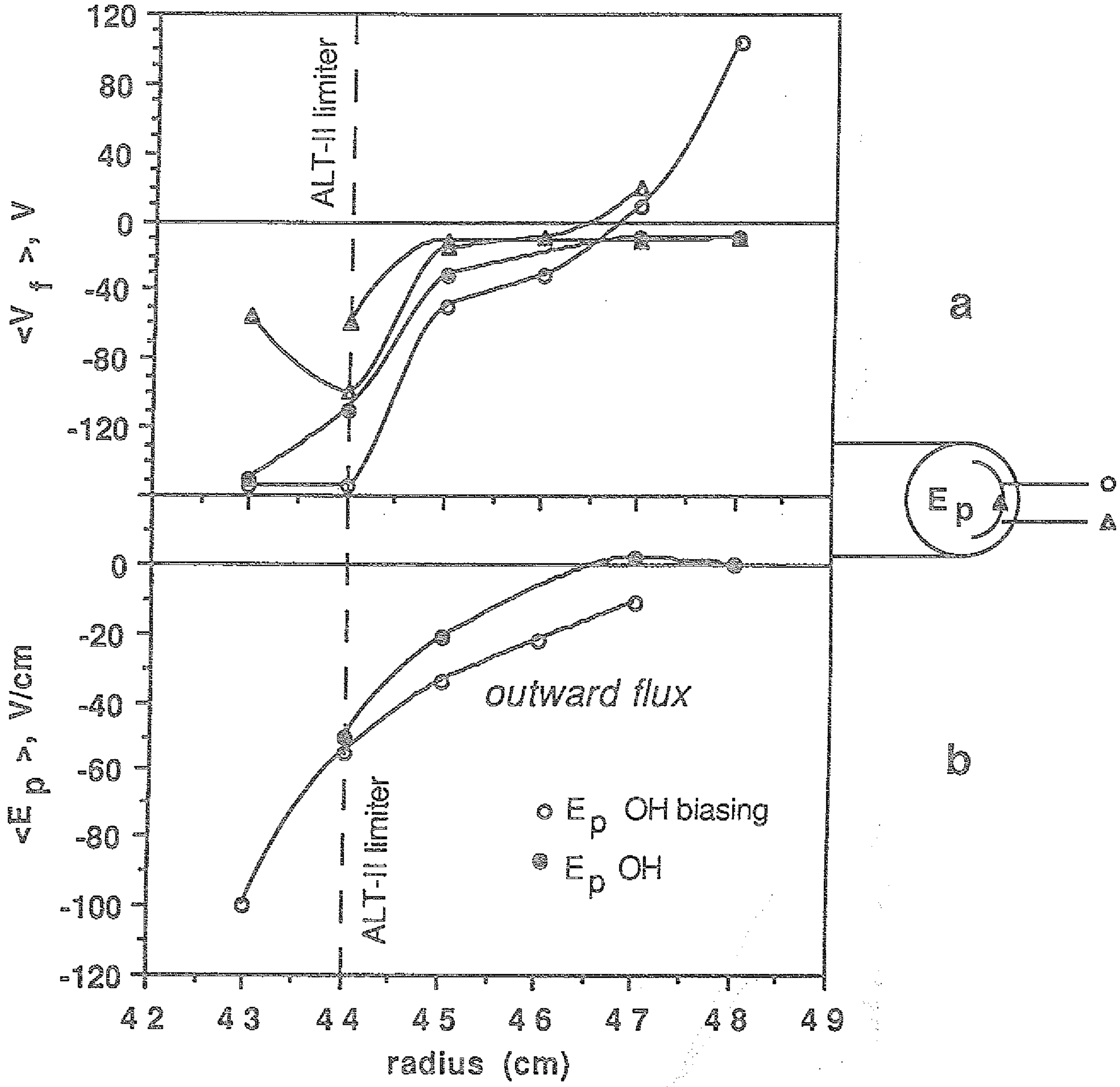

Fig.21: Radial profiles of (a) the time-averaged floating potential U_f and (b) the time-averaged poloidal electric field E_p in ohmic discharges without biasing (solid) and with six of eight segments of the ALT-II belt biased to -180 V (open; blades 4 and 8 grounded to the TEXTOR vessel).

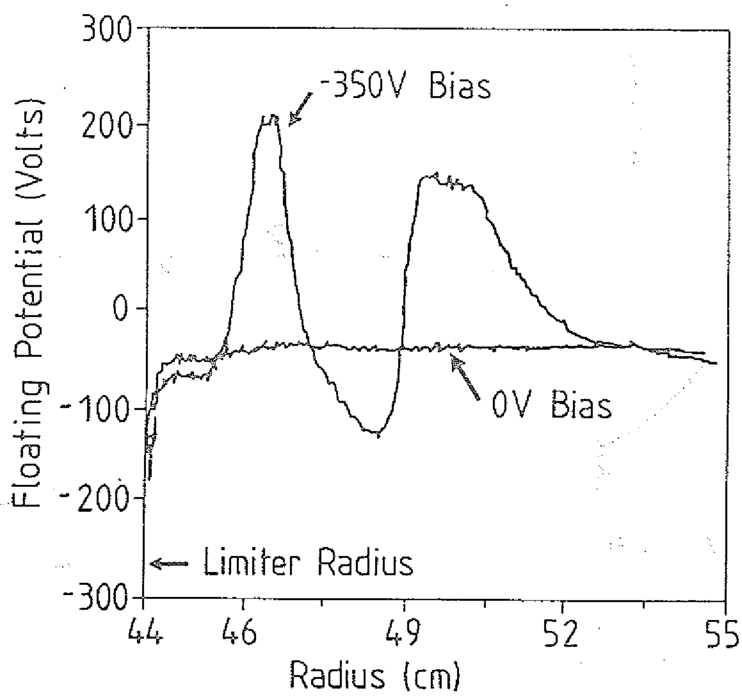

a

Edge Density Profiles During Ohmic

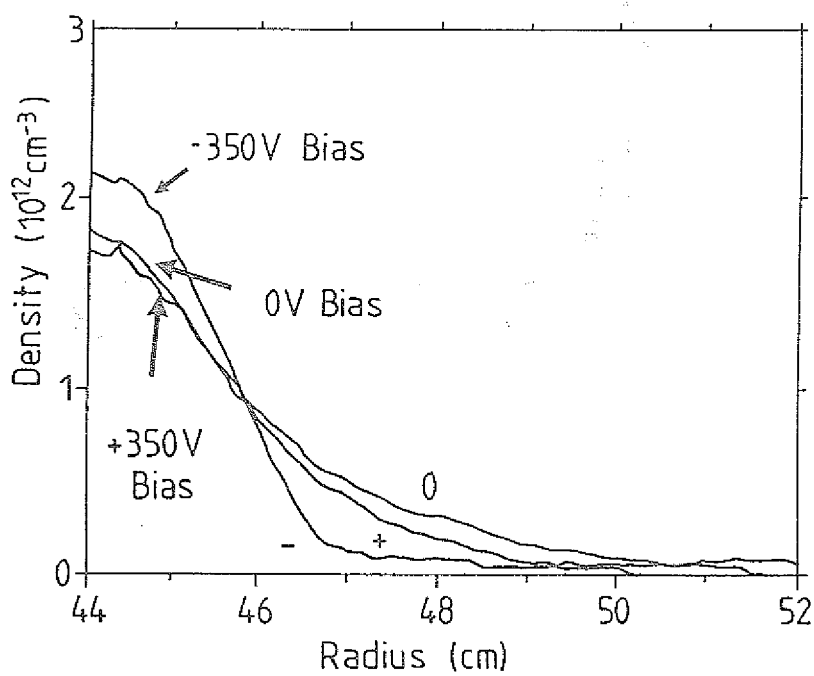

b

Fig.22: (a) Radial profiles of time–averaged floating potential U_f for ohmic discharges with 0 V and -350 V bias of the ALT–II toroidal belt as measured by the UCLA fast reciprocating probe. (b) Radial profiles of the edge plasma density, obtained with the thermal Lithium beam diagnostic, in unbiased and ±350 V biased ohmic discharges.

FORSCHUNGSZENTRUM JÜLICH GmbH

KFA

Jül-2432
January 1991
ISSN 0366-0885